

# Particle Simulation of Drift Waves in a Sheared Magnetic Field

R. D. Sydora, J. N. Leboeuf and T. Tajima  
Institute for Fusion Studies  
University of Texas  
Austin, Texas 78712

## ABSTRACT

Electrostatic properties of density gradient drift waves (the universal mode) in a sheared magnetic field are studied using a two-and-one-half dimensional particle code. For the case of a single rational surface, the drift waves are found to be stable with an eigenmode structure that matches the linear theoretical prediction as long as the ion resonance layer is well within the system. This applies to both even and odd parity modes with respect to the rational surface. The dependence on various parameters such as the shear length is examined.

## I. INTRODUCTION

The theoretical study of collisionless electrostatic drift waves driven by a density gradient (the universal mode), in a sheared magnetic field, was initiated many years ago.<sup>1-3</sup> It is now theoretically argued that within the framework of linear theory, absolutely unstable eigenmodes do not exist in slab geometry with a single rational surface in the absence of temperature gradients.<sup>4-6</sup> The stability of the universal mode in these latter treatments<sup>4-6</sup> is due to the inclusion of nonresonant electrons in the region about the mode rational surface. According to Refs. 7-11 convective amplification of drift wave packets can occur, however, for modes near marginal stability and for sufficiently weak shear.

Aside from subtle linear stability properties, the drift wave could easily exhibit highly nonlinear behavior. In order to investigate this important and subtle physics problem, particle simulations of drift instabilities were initiated in the seventies by Lee, Okuda and coworkers.<sup>12-14</sup> Their pioneering effort was successful in verifying the linear theory of drift instabilities in a shearless slab model. They found that quasilinear flattening of the density profile saturated the instability. Their simulations with a sheared magnetic field did not show the complete stabilization of the instability for a wide range of shear strengths. The eigenmode structure predicted by linear theory<sup>4-6</sup> was not observed and in the strongly sheared cases ( $L_s/L_n \lesssim 28$ ), "unstable local transients" dominated the simulations.<sup>14</sup> In the weaker shear cases ( $L_s/L_n > 28$ ) much higher fluctuation levels were observed.

As far as applications to tokamak plasmas are concerned, the sheared slab model with a single mode rational surface might not be considered of interest since three-dimensional effects<sup>15</sup> and toroidal geometry<sup>16</sup> may allow for possible absolute instability. Nevertheless, particle simulations of drift waves in a sheared slab with single rational surface have yet to be reconciled with linear theory. Also, the convective amplification of drift wave packets is still an open question. For example, the amplification may be at such high levels that nonlinear effects could occur prior to attainment of the predicted value.

We have carried out several simulations of density gradient driven drift waves in order to clarify the above questions. Our simulations are similar to previous ones in that we use the guiding center electron, full ion dynamics, electrostatic particle algorithm.<sup>17</sup> In order to simplify our analysis, an exponential density gradient profile is used in the direction perpendicular to the magnetic field and shear is incorporated by having the magnetic field vary linearly along the density gradient. We impose boundary conditions on the electrostatic potential at the endpoints of the simulation domain so as to allow only odd or even parity drift eigenmodes with respect to the rational surface. These various combinations allow us to test the effect of simulation boundary conditions on the drift waves. We consider systems with strong ( $L_s/L_n \lesssim 28$ ) and weak ( $L_s/L_n > 28$ ) shear and choose the shear scale length as well as rational surface position so that the ion resonance ( $x_i \approx \omega_* L_s / k_y v_i$ ) is always within the system ( $x_i < L_x$ ) unless specified otherwise. This will ensure that in our model the wave energy supplied at the electron resonance ( $x_e \approx \omega_* L_s / k_y v_e$ ) is absorbed

at the ion resonance ( $x_i$ ). In this way, we can hope to match the outgoing wave boundary condition of the linear theory,<sup>4-6</sup> which reflects the damping of wave energy at the ion resonance layer (the ion shear damping). In the strong shear cases ( $L_s/L_n \lesssim 28$ ) we would like to find out if the simulation system supports the predicted, linearly stable eigenmodes in the steady state, i.e. over long simulation time scales. For weak shear ( $L_s/L_n > 28$ ) the electron and ion resonances are more separated and it is of interest to observe the eigenmode formation at early times.

The organization of this paper is as follows. The simulation configuration, model parameters and diagnostic methods are presented in Sec. II. The linear theory of drift waves is briefly outlined in Sec. III and simulation results for strongly sheared as well as weakly sheared systems are given in Secs. IV and V, respectively. A discussion of the results and conclusions are presented in Sec. VI.

## II. SIMULATION MODEL

We describe the two-dimensional sheared plasma slab configuration with a single rational surface and its simulation realization in this section. The plasma parameters are defined as well as some of the diagnostic methods used to analyze the results.

The model used in the simulation is a two-and-one-half dimensional (spatial dimensions  $(x, y)$ , and velocity dimensions  $(v_x, v_y, v_z)$ ) electrostatic particle algorithm.<sup>17</sup> The initial configuration is shown in Fig. 1. The plasma is confined between two boundaries located at  $x = 0$  and  $x = L_x$ . In the  $y$ -direction the system is periodic with

length  $L_y$ . A strong confining sheared magnetic field is externally imposed with

$$\underline{B} = B_0 \left[ \hat{z} + \left( \frac{x-x_0}{L_s} \right) \hat{y} \right], \quad (1)$$

where  $x_0$  defines the location of the rational surface and  $L_s$  is the shear length. Therefore the wavenumber along the magnetic field is expressed as

$$k_{\parallel} = \underline{k} \cdot \underline{B}/|\underline{B}| \approx k_y(x-x_0/L_s), \quad (2)$$

with  $k_y = 2\pi m/L_y$ ,  $m = 0, \pm 1, \dots, \pm L_y/2$ . The plasma is assumed to initially have an exponential density profile

$$n(x) = n_0 \kappa L_x \{ \exp(-\kappa x) / [1 - \exp(-\kappa L_x)] \}. \quad (3)$$

This profile gives a constant density gradient scale length  $L_n (\equiv 1/\kappa)$ , with  $\kappa = -n'(x)/n$ . There is no temperature gradient imposed initially.

The boundary condition imposed on the electrostatic potential at the endpoints  $x = 0$  and  $x = L_x$  are of two types. The first requires  $\phi(0) = 0 = \phi(L_x)$  which allows for odd parity modes with respect to the endpoints in the simulation. The second type used is  $\partial\phi/\partial x(x=0) = 0 = \partial\phi/\partial x(x=L_x)$  which corresponds to even parity modes. Therefore the eigenmode parity, with respect to the rational surface, is determined by its position relative to the endpoints. For example, if the rational surface is placed at  $x = 0$  and odd parity

modes are imposed with respect to the boundary points, then the eigenmodes are odd with respect to the rational surface.

For particle motion, the guiding center approximation for electrons is used and full ion dynamics are followed. The particles are specularly reflected at the walls in such a way as to eliminate the sheath currents which may occur.<sup>18</sup> Reflection of particles implies that there is no mechanism for net energy loss in the system. The system size used for the strong shear simulations is  $L_x \times L_y = 64\Delta \times 32\Delta$  with unit grid spacing  $\Delta$ . The average number density is  $n_0 = 16/\Delta^2$ , ion to electron mass ratio  $m_i/m_e = 100$ , temperature ratio  $T_i/T_e = 1$ , and electron Debye length  $\lambda = 2.5\Delta$  or electron thermal velocity  $V_e = 2.5\omega_{pe}\Delta$  where  $\omega_{pe}$  is the electron plasma frequency. The ion Larmor radius is  $\rho_i = 2.5\Delta$  where  $\rho_i = v_i/\omega_{ci}$  and  $v_i = (T_i/m_i)^{1/2}$  with  $\omega_{ci}$  the ion cyclotron frequency,  $\omega_{ce}/\omega_{pe} = 10$ , and time step  $\omega_{pe}\Delta t = 2-4$ . The density gradient scale length is  $L_n = 1/\kappa = 14.3\Delta$  and  $\kappa = 0.07\Delta^{-1}$ . The shear scale length is varied from  $L_s = 400\Delta(\omega_{pe}\Delta t = 4)$  to  $L_s = 200\Delta(\omega_{pe}\Delta t = 2)$ . The rational surface position,  $x_0$ , has been placed either at  $x_0 = 0$  or at  $x_0 = L_x/2 = 32\Delta$ . The system described above supports discrete wavenumbers  $k_y\rho_i = 0.49m$ ,  $m = 0, \pm 1, \dots, \pm L_y/2$ , where  $m$  is the mode number in the y-direction. The electron diamagnetic drift frequency defined as  $\omega_* = k_y c T_e / L_n e B$  is  $\omega_*/\omega_{pe} = 0.0086m$ . The simulations have been carried out for  $\omega_* t = 70$  ( $m = 1$ ).

The diagnostics involve the determination of the frequencies of potential fluctuations for a fixed  $k_y\rho_i$  at various positions in the x-direction. They are obtained from power spectra of the potential by

the maximum entropy correlation technique.<sup>19</sup> The equation for the power spectral intensity is given by

$$I_{k_y}(x, \omega) = \int_{-\infty}^{\infty} d\tau A_{k_y}(x, \tau) \exp(i\omega\tau) , \quad (4)$$

where the correlation function is

$$A_{k_y}(x, \tau) = \lim_{T \rightarrow \infty} \frac{1}{T} \int_0^T dt \tilde{\phi}_{k_y}(x, t) \tilde{\phi}_{k_y}^*(x, t+\tau)$$

for a lag time  $\tau$ . The spatial structure of the fluctuations at a particular frequency is best analyzed by an interferogram technique<sup>20</sup> which is a correlation of the plasma potential at a particular  $k_y \rho_i$  for a fixed frequency,  $\omega_0$ , determined by the power spectra. The following quantity is computed

$$C_{k_y}(x, \tau) = \frac{1}{T} \int_0^T \tilde{\phi}_{k_y}(x, t+\tau) \sin(\omega_0 t) dt , \quad (5)$$

where  $\tau$  is a variable lag time and  $T$  the total time of integration.

### III. LINEAR THEORY

In this section we briefly review the linear theory of drift waves. The governing equation for potential fluctuations of the form  $\tilde{\phi} = \tilde{\phi}(x) \exp[i(k_y y - \omega t)]$  can be written as

$$\left[ 1 + \eta + \left( 1 - \frac{\omega_*}{\omega} \right) \xi_e Z(\xi_e) + \left( \eta + \frac{\omega_*}{\omega} \right) \xi_i Z(\xi_i) I_0(b) e^{-b} \right] \tilde{\phi} = 0 , \quad (6)$$

where

$$\eta = T_e/T_i, \quad \xi_\alpha = \omega L_s / \sqrt{2} k_y (x - x_0) v_\alpha, \quad (\alpha = e, i), \quad b = (k_x^2 + k_y^2) \rho_i^2,$$

$Z$  is the plasma dispersion function<sup>21</sup> and  $I_0$  is the modified Bessel function. For  $k_x \rho_i \ll 1$  we can replace  $k_x$  by  $-i\partial/\partial x$  in Eq. (6) to obtain the eigenmode equation<sup>8,10</sup>

$$\tilde{\phi}'' + Q(\tilde{x}, \omega) \tilde{\phi} = 0, \quad (7)$$

where

$$Q(\tilde{x}, \omega) = \eta - k_y^2 \rho_s^2 + \frac{(1+\eta)(\frac{\omega}{\omega_*}) + (\frac{\omega}{\omega_*} - 1) \xi_e Z(\xi_e)}{(\frac{\omega}{\omega_*} + \frac{1}{\eta}) \xi_i Z(\xi_i)},$$

with  $\rho_s = \sqrt{\frac{T_e}{T_i}} \rho_i$  and  $\tilde{x} = x/\rho_s$ . The prime denotes differentiation with respect to  $\tilde{x}$ .

The electron and ion resonance locations,  $x_e$  and  $x_i$ , are determined from the condition  $\xi_\alpha \approx 1$ , so that  $x_e = \omega L_s / \sqrt{2} k_y v_e$  and  $x_i = \omega L_s / \sqrt{2} k_y v_i$  where  $\omega$  refers to the normal mode frequency. Equation (7) has been solved using a standard shooting code<sup>4,22</sup> method with the simulation parameters. The eigenfunctions for even and odd modes, with respect to the rational surface are displayed in Figs. 2(a) and 2(b), respectively, with  $k_y \rho_s = 0.49$ . The eigenfrequencies and damping rates for various values of  $k_y \rho_s$  are shown in Fig. 3. The real frequencies for odd and even parity were almost the same numerically and therefore only the values for the even parity are shown. In all



cases linear theory predicts stable, linearly damped modes for odd and even parity. It is also necessary to solve the local dispersion relation and it is simply obtained by setting  $k_x^2 = 0$  in Eq. (6).<sup>14</sup>

#### IV. SIMULATION RESULTS (STRONG SHEAR)

Various cases corresponding to different boundary conditions and different positions of the rational surface, as well as two different shear strengths,  $L_s/L_n = 14$  and 28 will be presented. We consider both odd and even parity modes. The even parity mode is the ordinary universal mode of drift waves. The odd mode parity is often neglected because it is a heavily damped mode as is seen in Fig. 3.

##### Case 1: Odd parity modes with rational surface $x_0 = 0$

This simulation is carried out with  $\phi(0) = 0 = \phi(L_x)$  boundary conditions. With rational surface at  $x_0 = 0$ , we are simulating a half-space which supports odd parity modes only, i.e.  $\tilde{\phi}(x) = \sum_n \phi_n \sin(n\pi x/L_x)$ ,  $n = 0, \pm 1, \dots, \pm L_x/2$ . A value of  $L_s/L_n = 28$  is used and with  $\omega_*/\omega_{pe} = 0.0086$  the ion resonance location is at  $x_i(\omega_*) = 49.5\Delta$  which gives  $x_i(\omega) < x_i(\omega_*) < L_x$ , where  $\omega$  is the eigenfrequency. Therefore the ion resonance layer is well within the system since  $L_x = 64\Delta$ . Note that  $x_i(\omega_*)$  evaluated at  $v_i$  is the most stringent condition to ensure the ion shear damping layer is within the simulation domain. Since ion Landau damping is maximum at  $v_i$ , the ion resonance location is well approximated by  $x_i(\omega)$ . The time evolution of the total electrostatic energy is shown in Fig. 4 and a weak instability is found to occur. An increase by a factor of two is observed from  $\omega_*t = 0 - 70$ . This increase is due to the enhancement of

mode  $k_y \rho_s = 0$ , the "ambipolar mode". Other modes with finite  $k_y \rho_s$  show no increase from their initial fluctuation levels and this is illustrated in Fig. 5. In this figure we have given the spatially averaged fluctuation level per mode since the eigenmode structure is nonlocal and we are attempting to observe net sustained growth of the fluctuations.

The local power spectrum of the fluctuations at positions  $x/\rho_s = 9.6$  and  $x/\rho_s = 12.8$ , corresponding to regions of maximum mode amplitude for  $k_y \rho_s = 0.49$ , are given in Fig. 6. The measured frequency,  $\omega/\omega_* \approx 0.9 \pm 0.03$  is a factor of two larger than the eigenfrequency  $\omega/\omega_* = 0.44$ . Figure 7 shows the agreement between frequencies at various x-positions using Eq. (4) and values obtained by solving the local dispersion relation [ $k_x^2 = 0$  in Eq. (6)]. This suggests that local fluctuations are prevalent and the theoretically predicted eigenmodes are not observed. A similar result was obtained by previous authors.<sup>14</sup>

#### Case 2: Even parity modes with rational surface $x_0 = 0$

The simulation parameters are identical to the previous case and the only difference is that  $\partial\phi/\partial x = 0$  boundary conditions are used at  $x = 0$  and  $x = L_x$ . With rational surface at  $x = 0$  only even modes given by  $\tilde{\phi} = \sum_n \phi_n \cos(n\pi x/L_x)$  are allowed in the simulation. According to linear theory these modes are stable and are less heavily damped than the odd parity.

The time evolution of the total electrostatic energy is depicted in Fig. 8. There is no observable increase in the total electrostatic energy or in the energy of the individual discrete modes, as shown in

Fig. 9. The electrostatic energy is dominantly in the  $m=0$  and  $m=1$  modes because finite particle size as well as shielding effects enter for  $m>1$ .

The power spectrum of the potential fluctuations for  $k_y \rho_s = 0.49$  is illustrated in Fig. 10. Figure 10(a) represents the power spectrum for all  $x$ -positions and Fig. 10(b) is the spectral intensity at  $x/\rho_s = 4$  where the spectral maximum occurs. The measured frequency is  $\omega/\omega_{*} = 0.43 \pm 0.02$  and this is in reasonable agreement with the shooting code result,  $\omega/\omega_{*} = 0.33$ , from Fig. 2(a). We note that the local theory gives a value of  $\omega/\omega_{*} = 0.7$  at  $x/\rho_s = 4$  as obtained from Fig. 7. The interferogram of the potential fluctuations at the measured frequency for mode  $k_y \rho_s = 0.49$ , is displayed in Fig. 11 along with the shooting code results. Good agreement is found for both the real and imaginary parts of the potential structure.

The results from this case indicate that an eigenmode structure is established and is stable, which is in agreement with the linear theory of the universal mode.<sup>4-6</sup> The long time evolution represents the steady state sustained by energy balance between "Cerenkov emission" of electron kinetic energy into the wave at the electron resonance and shear damping of the wave into parallel ion kinetic energy at the ion Landau resonance. Because of this energy exchange from electrons to waves to ions, there is a net energy flow even though the eigenmodes are stable. In fact, we observe that the electron momentum in the  $y$ -direction, near  $x = x_e$ , gives up a finite value in the electron diamagnetic drift direction. To quantitatively estimate the momentum transfer we use the quasilinear value and, assuming resonant diffusion is dominant, the diffusion coefficient is given by

$$D_x = \left(\frac{c}{B}\right)^2 \sum_k k_y^2 |\phi_k|^2 \pi \delta(k_{\parallel} v_{\parallel} - \omega_k) , \quad (8)$$

using the fact that  $\gamma \ll \omega$  and  $\omega < \omega_k$ . The evolution of the average distribution is governed by

$$\frac{\partial f_0}{\partial t} = \frac{\partial}{\partial x} \left( D_x \frac{\partial f_0}{\partial x} \right) , \quad (9)$$

and the rate of change of momentum is

$$\frac{d}{dt} \int f_0 v_{\parallel} dv_{\parallel} \approx \pi \sum_k \left| \frac{e \phi_k}{T_e} \right|^2 \frac{\omega_k}{k_{\parallel}^2} \omega_k^2 f_0 \left( \frac{\omega_k}{k_{\parallel}} \right) . \quad (10)$$

For fluctuation levels of  $|e \phi_k / T_e| \sim 10^{-3} - 10^{-2}$  we obtain

$$\frac{d\langle v_{\parallel} \rangle / v_e}{d(\omega_{pe} t)} \sim 2 \times 10^{-6} ,$$

which is compared with the observed value of  $10^{-6}$ . The ion momentum in the y-direction, near  $x=x_i$ , acquires a finite value in the direction of the electron diamagnetic drift as a result of the wave-particle interaction. Equation (10) also gives agreement within a factor of two for the rate of change of momentum in the ions. The energy transport and momentum transport in the x-direction is, therefore, nonzero even in the absence of instability (i.e., beyond the collisional contributions).

Case 3: Even parity modes with respect to  $x_0 = L_x/2$

The simulation parameters are identical to the previous cases except that  $L_s/L_n = 14$  is used in order to keep  $x_i < L_x$ . In this case  $x_i(\omega_*) = 57\Delta < L_x = 64\Delta$  and  $\phi = 0$  boundary conditions are used at  $x = 0$  and  $L_x$ . This allows modes of the form  $\tilde{\phi}(x) = \sum_{n'} \phi_{n'} \sin(n'\pi x/L_x)$ , however, we keep only the modes with  $n' = 2n - 1$ ,  $n = \pm 1, \pm 2, \dots, \pm L_x/2$  in the simulation. This insures that only modes with even parity with respect to the rational surface are present. The purpose of this case and the next is to make sure the results of Case 2 were not influenced by any deleterious boundary effects.

As was found in Case 2, no increase in the total electrostatic energy or the individual mode energies is observed. Contours of the electrostatic potential taken at  $\omega_* t = 30$  are shown in Fig. 12. Note the symmetry of the potential with respect to the rational surface. The power spectrum of the potential fluctuations at  $(x-x_0)/\rho_s = 3.2$  is displayed in Fig. 13 and the measured frequency is  $\omega/\omega_* = 0.35 \pm 0.03$  which is to be compared with the shooting code result  $\omega/\omega_* = 0.36$ . The stable drift wave eigenfunction for  $k_y \rho_s = 0.49$  is given in Fig. 14 and the agreement between simulation and theory is excellent. Note the evanescent character of the mode away from the rational surface and that the ion resonance, located at  $x_i/\rho_s = 8.65$ , is the cause of this spatial decay.

Our simulation results in Cases 2 and 3 establish the existence of drift wave eigenmodes of linear theory for even parity, irrespective of the position of the rational surface with respect to the simulation boundaries.

Case 4: Odd parity modes with respect to  $x_0 = L_x/2$

The simulation parameters used are identical to the previous case. The shear scale length is  $L_s/L_n = 14$  and  $\phi(0) = 0 = \phi(L_x)$ . The potential fluctuations are described by  $\tilde{\phi} = \sum_n \phi_n' \sin(n'\pi x/L_x)$  and only modes with  $n' = 2n$ ,  $n = \pm 1, \dots, \pm L_x/2$  are allowed in the simulation. Therefore, only modes with odd parity with respect to the rational surface are described by the code.

As was found in the previous case, the potential fluctuations are stable and the time history of the total electrostatic energy shows no enhancement above the initial noise level. An energy per mode analysis, gives a similar result. The power spectrum of the potential fluctuations for mode  $k_y \rho_s = 0.49$ , averaged over several x-positions near the rational surface, is displayed in Fig. 15 and a mode frequency of  $\omega/\omega_* = 0.33 \pm 0.1$  is observed which agrees well with the shooting code result of  $\omega/\omega_* = 0.36$ . An interferogram of the potential fluctuations for  $k_y \rho_s = 0.49$  is illustrated in Fig. 16(a) along with the wave function of the shooting code in Fig. 16(b). Again, excellent agreement is obtained between the theory and simulation.

From the results of Cases 1 and 4, for odd drift wave parity, we conclude that the particle simulation model gives the expected linear eigenmode structure only when the rational surface does not coincide with the simulation boundaries.

To conclude this section we illustrate two situations which do not produce the eigenmodes predicted by linear theory. In the first situation, let us consider the parameters and boundary conditions of Case 3. As has been discussed, if only even modes with respect to the rational surface are kept, the simulation and theoretical wave

functions agree very well. However, if both even and odd parity modes are kept, the wave functions obtained from the simulation does not match the linear theoretical result. This is shown in Fig. 17. The nonsymmetry of the wave function arises from the mixture of parities retained in the simulation. The measured frequency agrees very well with the eigenmode frequency, which suggests that the odd parity mode gives only a small contribution to the dominant even modes.

A second situation which can produce undesirable results is the parameter regime where the ion resonance layer lies outside the simulation domain or is very near the boundaries. Once again, Case 3 is chosen but the shear is allowed to vary in order to demonstrate what can occur when  $x_i(\omega_*) > L_x$ . For shear strength of  $L_s/L_n = 14$ , Fig. 18(a) illustrates that the fluctuation level remains at thermal noise over the entire length of the run and  $x_i(\omega_*) = 41\Delta < L_x$ . As is evident from Fig. 18(b) the fluctuation level is enhanced above thermal noise when  $L_s/L_n = 28$  and  $x_i(\omega_*) = 81\Delta > L_x$ . This enhancement occurs because the boundary at  $L_x$  affects the outward propagation of energy and does not allow for the spatial decay of the wave function. It is important to note that the fluctuations do not grow because the electron and ion resonances are more separated. This can be seen by comparing the results of this case with Case 2. In Case 2 the fluctuations remain at the thermal noise level even though the electron and ion resonances are the same distance apart as in the above situation.

## V. SIMULATION RESULTS (WEAK SHEAR)

In this section we consider systems with weakly sheared magnetic fields ( $L_s/L_n \geq 30$ ). When the magnetic shear becomes very weak, the electron and ion resonance regions become well separated spatially and the eigenfunction is highly oscillatory. If the resonances are well separated one expects that there will be a finite time before shear damping by the ions occurs. During this finite lag time the local growth of the drift wave eigenmode could be large enough to cause modification of the equilibrium density profile. Therefore, the purpose of this section is to determine whether or not this indeed does occur and to establish the resultant fluctuation levels of the eigenmodes in weakly sheared systems.

Two separate cases have been considered. In the first case the simulation parameters used were,  $L_x \times L_y = 128\Delta \times 32\Delta$ ,  $n_0 = 16/\Delta^2$ ,  $m_i/m_e = 400$ ,  $T_e/T_i = 4$ ,  $\omega_{ce}/\omega_{pe} = 10$ ,  $\lambda_e = 2.5\Delta$ ,  $a_x = a_y = 1.5$ ,  $\omega_{pe}\Delta t = 4$ ,  $\kappa = 1/L_n = .035$ ,  $k_y\rho_i = 0.5m$  and  $\omega_*/\omega_{pe} = .00437m$  where  $m = 0, \pm 1, \dots, \pm L_y/2$ . The shear strength was chosen to be  $L_s/L_n = 70$  and the rational surface location at  $x = 0$ . The boundary condition  $\phi'(0) = 0 = \phi'(L_x)$  was chosen, which corresponds to even parity modes with respect to the rational surface; this is the universal mode of interest.

A shooting code was used to determine the eigenvalue and eigenfunction with the above parameters. The wave function is displayed in Fig. 19 and the oscillatory character of the mode is clearly seen. The eigenvalue is given by  $(\omega/\omega_* = 0.167$ ,  $\gamma/\omega_* = -.46 \times 10^{-4})$  for  $k_y\rho_s = 0.98$ , which indicates the mode is near marginal stability.



From the simulation, the potential fluctuation levels of modes  $k_y \rho_s = 0$  and  $k_y \rho_s = 0.98$  versus time are shown in Figs. 20(a) and 20(b), respectively. The fluctuation level of  $k_y \rho_s = 0.98$  increases by a factor of two above the initial noise level and saturates at  $\omega_* t \approx 7$ . At this time the energy in mode  $k_y \rho_s = 0$  begins to increase and saturates near the end of the run. This increase corresponds to a flattening of the density profile locally near the electron resonance. In order to establish the spatial characteristics of the mode  $k_y \rho_s = 0.98$ , a space-time diagram is constructed and illustrated in Fig. 21(a). The x-axis represents the spatial coordinate, the y-direction is the time axis and mode amplitude,  $e\phi/T$ , is in the z-direction. The electron resonance, denoted by  $x_e$ , is represented by the dashed line and the ion resonance is outside the simulation domain, in the sense that the evaluated  $x_i$  is given by  $x_i(\omega_*) > L_x > x_i(\omega_0)$ , where  $\omega_0$  is the eigenfrequency. The mode begins to grow locally at the electron resonance and saturates at  $\omega_* t \approx 7$ . After saturation the electron density profile begins to flatten about  $x_e$  and the mode amplitude of  $k_y \rho_s = 0.98$  decreases at  $x_e$  and increases in amplitude at  $x > x_e$ . The mode amplitude rises slightly at the electron resonance and continues to oscillate with diminished amplitude. In order to determine the frequency of oscillation near the electron resonance, a power spectrum is computed locally at  $x = x_e$  and from Fig. 21(b) a frequency of  $\omega/\omega_* \approx 0.32 \pm .03$  is measured which is larger than the eigenmode frequency  $\omega/\omega_* = 0.167$ . The local frequency, determined by setting  $k_x^2 = 0$  in Eq. (6), is found to be  $\omega/\omega_* = 0.39$ . Therefore the local frequency appears to agree more closely with the measured simulation value. This is understandable because with  $x_i(\omega)$ , where  $\omega$

is the measured frequency, outside the system, the outgoing wave boundary condition which is necessary to produce the eigenmode is not realized.

For the second case, the parameters chosen previously were used except for  $m_i/m_e = 100$ ,  $\lambda_e = 1.0\Delta$ ,  $k_y\rho_i = 0.098m$  and  $\omega_*/\omega_{pe} = 0.00068m$  where  $m = 0, \pm 1, \dots, \pm L_y/2$  so that  $x_1(\omega) < x_1(\omega_*) < L_x$ . The mode corresponding to  $k_y\rho_s = 0.78$  showed a factor of two increase above its initial noise level over the length of the run while all other modes remained at their initial fluctuation levels. This is illustrated in Fig. 22(b). The equilibrium level which the modes reach is related to convective losses or redistribution of equilibrium thermal energy due to the eigenmode. From Fig. 22(a) it appears the growth in  $k_y\rho_s = 0.78$  was not sufficient to modify the equilibrium electron density profile. A space-time diagram of  $k_y\rho_s = 0.78$  is given in Fig. 23(a) and the maximum amplitude is  $e\phi/T \approx 0.006$ . Note the oscillatory structure of the mode near the electron resonance,  $x_e$ , and the spatial decay of the mode amplitude at the ion resonance,  $x_i$ . The local power spectrum, shown in Fig. 23(b) and taken at  $x/\rho_s = 20$ , indicates the frequency peaks near the eigenmode frequency,  $\omega/\omega_* = 0.3$ , obtained from the shooting code. The local frequency is  $\omega/\omega_* = 0.65$ . The simulation frequency is measured by using data over the entire length of the run. Therefore the main contribution to the measured frequency comes from the flat portion of the mode energy versus time curve of Fig. 22(b). After  $t = 1.5\omega_*^{-1}$  the eigenmode structure appears to have been set up.

## VI. SUMMARY

In this work we have investigated the stability of drift waves in the sheared slab model using the methods of particle simulation. We have considered a variety of boundary conditions at the endpoints of the simulation domain, rational surface positions with respect to the boundaries, i.e. different drift wave parities, different ion resonance layer locations and shear strengths. The principal results can be summarized as follows.

For strongly sheared magnetic fields ( $L_s/L_n \lesssim 28$ ), the stable eigenmodes predicted by linear theory are found to be present as long as the ion resonance layer is well within the simulation domain. The eigenmodes are observed for the even parities irrespective of the rational surface position. They are also observed for the odd parity whenever the rational surface position does not coincide with the simulation boundary. The stable eigenmodes of linear theory are not found when these two positions coincide and this is probably a result of boundary effects on the drift wave eigenmode parity which is present only in this situation. These effects may arise because the mode parity is imposed on the background as well as the perturbed potential and density.

A number of runs were carried out in systems with weak magnetic shear. It was found that when the electron and ion resonances are well enough separated, local growth near the electron resonance is sufficient to modify the equilibrium density profile which in turn limits the growth of the mode. With weak shear and ion resonance layer within the simulation domain a slight increase in the fluctuation level

of the mode with  $k_y \rho_s \approx 1$  occurred; however, the eigenmode frequency predicted by linear theory resulted over the entire length of the run.

#### ACKNOWLEDGMENTS

The authors would like to thank F. Brunel, V. Decyk, P. H. Diamond, T. Kamimura, W. W. Lee, M. N. Rosenbluth and P. W. Terry for many helpful discussions. We would also like to thank Dale Humanic for making his maximum entropy power spectral technique available to us and to J. Sedlak for his assistance with the shooting code results. This work was supported by the U.S. Department of Energy, under grant DE-FG05-80-ET-53088 and the National Science Foundation under grant ATM-82-14730.

REFERENCES

1. N. Krall and M. N. Rosenbluth, Phys. Fluids 8, 1488 (1965).
2. P. H. Rutherford and E. A. Frieman, Phys. Fluids 10, 1007 (1967).
3. L. D. Pearlstein and H. L. Berk, Phys. Rev. Lett. 23, 220 (1969).
4. D. W. Ross and S. M. Mahajan, Phys. Rev. Lett. 40, 324 (1978).
5. K. T. Tsang, P. J. Catto, J. C. Whitson, and J. Smith, Phys. Rev. Lett. 40, 327 (1978).
6. T. M. Antonsen, Phys. Rev. Lett. 41, 33 (1978).
7. L. Chen, P. N. Guzdar, R. B. White, P. K. Kaw, and C. Oberman, Phys. Rev. Lett. 41, 649 (1978).
8. Y. C. Lee and L. Chen, Phys. Rev. Lett. 42, 708(1979).
9. F. L. Hinton and M. N. Rosenbluth, Phys. Fluids 23, 528 (1980).
10. W. M. Nevins and L. Chen, Phys. Fluids 23, 1973 (1980).
11. R. E. Waltz, W. Pfeiffer, and R. R. Dominguez, Phys. Fluids 23, 985 (1980).
12. W. W. Lee and H. Okuda, Phys. Rev. Lett. 36, 870 (1976).
13. W. W. Lee, Y. Y. Kuo, and H. Okuda, Phys. Fluids 21, 617 (1978).
14. W. W. Lee, W. M. Nevins, H. Okuda, and R. B. White, Phys. Rev. Lett. 43, 347 (1979).
15. S. P. Hirshman and K. Molvig, Phys. Rev. Lett. 42, 648 (1979).
16. R. J. Hastie, K. W. Hesketh, and J. B. Taylor, Nucl. Fusion 19, 1223 (1979); L. Chen, M. S. Chance, and C. Z. Cheng, Nucl. Fusion 20, 901 (1980); C. Z. Cheng and L. Chen, Phys. Fluids 23, 1770 (1980).
17. W. W. Lee and H. Okuda, J. Comp. Phys. 26, 139 (1975).
18. H. Naitou, S. Tokuda, and T. Kamimura, J. Comp. Phys. 33, 86 (1979).
19. J. P. Burg, Ph.D. thesis, Stanford University (1975); D. Humanic and J. M. Dawson, private communication.
20. V. K. Decyk, G. J. Morales, and J. M. Dawson, Phys. Fluids 23, 826 (1980).

21. B. D. Fried and S. D. Conte, The Plasma Dispersion Function (Academic Press, NY, 1961).
22. N. T. Gladd and W. Horton, Jr., Phys. Fluids 16, 879 (1973);  
D. W. Ross and S. M. Mahajan, Phys. Fluids 22, 294 (1979).

## FIGURE CAPTIONS

Fig. 1

Schematic of the particle simulation configuration and model.

Fig. 2

Linear theory results illustrating real (full curve) and imaginary (dotted curve) parts of wavefunction  $\phi(x)$  as a function of  $x/\rho_s$  for (a) even parity modes and (b) odd parity modes. Parameters used are  $L_s/L_n = 28$ ,  $m_i/m_e = 100$ ,  $T_i/T_e = 1$  and  $L_n^{-1} = 0.07$ .

Fig. 3

Linear theory results for real and imaginary parts of eigenmode frequency  $\omega/\omega_*$  and  $\gamma/\omega_*$  as a function of  $k_y\rho_s$  for even and odd parity modes with same parameters as Fig. 2. Only the real frequency for the even parity is shown because the odd parity has nearly the same numerical value.

Fig. 4

Time evolution of the total electrostatic energy normalized to the total kinetic energy for Case 1.

Fig. 5

Time evolution of the spatially averaged mode amplitude for (a)  $k_y\rho_s = 0$  and (b)  $k_y\rho_s = 0.49$  in Case 1.

Fig. 6

Power spectra of potential  $\phi_{k_y}(x)$  as a function of real frequency  $\omega/\omega_*$  for (a)  $k_y\rho_s = 0.49$  at  $x/\rho_s = 9.6$  and (b)  $k_y\rho_s = 0.49$  at  $x/\rho_s = 12.8$  for Case 1. The eigenmode frequency from linear theory ( $\omega/\omega_* = 0.44$ ) is indicated by an arrow on the frequency axis.

Fig. 7

Real frequency,  $\omega/\omega_*$ , as a function of  $x/\rho_s$  for mode  $k_y\rho_s = 0.49$ . Theoretical result is indicated by full curve and dots represent simulation values for Case 1 parameters.

Fig. 8

Time evolution of total electrostatic energy normalized to total kinetic energy for Case 2 parameters.

Fig. 9

Time evolution of the spatially averaged mode amplitude for (a)  $k_y \rho_s = 0$  and (b)  $k_y \rho_s = 0.49$  in Case 2.

Fig. 10

Power spectra of the potential  $\phi_{k_y}(x)$  as a function of real frequency  $\omega/\omega_*$  for mode  $k_y \rho_s = 0.49$ . (a) Power spectrum,  $I(\omega)$  over all points in space ( $x/\rho_s$ ). The eigenmode frequency  $\omega/\omega_* = 0.324$  is indicated by an arrow on the frequency axis.  $x_e$  and  $x_i$  label the electron and ion resonance points, respectively. (b) Power spectrum,  $I(\omega)$  taken at  $x/\rho_s = 4$ . The arrow on the frequency axis indicates the local frequency  $\omega/\omega_* = 0.7$ . The results are for Case 2.

Fig. 11

The real and imaginary parts of the wave function obtained from theory and simulation (interferogram method) with  $\omega/\omega_* = 0.32$  for mode  $k_y \rho_s = 0.49$ . The results are for Case 2 parameters.

Fig. 12

Electrostatic potential and mode amplitude at selected time,  $\omega_* t = 24.5$ . (a) Electrostatic potential contours in  $x$ - $y$  plane and (b) mode amplitude of  $k_y \rho_s = 0$  as a function of  $(x - x_0)\rho_s$ , where  $x_0 = L_x/2$  is mode rational surface position for Case 3.

Fig. 13

Power spectra of mode  $k_y \rho_s = 0.49$  versus real frequency  $\omega/\omega_*$  taken at local position  $(x - x_0)/\rho_s = 3.2$  for Case 3. The arrow indicates the value of the local frequency  $\omega/\omega_* = 0.7$ .



Fig. 14

The real and imaginary parts of the wave function obtained from theory and simulation for Case 3. This is for mode  $k_y \rho_s = 0.49$ .

Fig. 15

Power spectra of mode  $k_y \rho_s = 0.49$  versus real frequency  $\omega/\omega_*$  taken as average over spatial positions  $(x - x_0)\rho_s = 2.0 - 5.0$ . The local frequency from linear theory,  $\omega/\omega_* = 0.7$ , is indicated by the arrow. This is for Case 4 parameters.

Fig. 16

The real and imaginary parts of the wave function obtained from (a) theory and (b) simulation. The results are for mode  $k_y \rho_s = 0.49$  in Case 4.

Fig. 17

Real and imaginary parts of the wave function for mode  $k_y \rho_s = 0.49$  with parameters the same as Case 3, but with mixture of odd and even parity with respect to rational surface.

Fig. 18

Time evolution of total electrostatic energy normalized to total kinetic energy for parameters of Case 3 and (a)  $L_s/L_n = 14$  which keeps ion resonance within system and (b)  $L_s/L_n = 28$  which moves resonance outside simulation domain.

Fig. 19

Wave function obtained from shooting code for weak shear case,  $L_s/L_n = 70$ , and even parity. Solid curve is the real part and dotted line is the imaginary part of the wave function.

Fig. 20

Time evolution of the spatially averaged mode amplitudes for (a)  $k_y \rho_s = 0$  and (b)  $k_y \rho_s = 0.98$  in weak shear case,  $L_s/L_n = 70$ , with ion resonance outside system.

Fig. 21

Space-time diagram and power spectra of mode  $k_y \rho_s = 0.98$ .  
(a) Mode amplitude,  $|e\phi/T|$ , versus  $(x/\rho_s)$  and time  $(\omega_* t)$ . Electron resonance is labeled by  $x_e$ . (b) Power spectrum taken at  $x = x_e$ .

Fig. 22

Time evolution of the spatially averaged mode amplitude for  
(a)  $k_y \rho_s = 0$  and (b)  $k_y \rho_s = 0.78$  in weak shear case with ion resonance within simulation domain.

Fig. 23

Space-time diagram and power spectra of mode  $k_y \rho_s = 0.78$ .  
(a) Mode amplitude,  $|e\phi/T|$ , versus space  $(x/\rho_s)$  and time  $(\omega_* t)$ . Electron and ion resonances are indicated by  $x_e$  and  $x_i$ , respectively.  
(b) Local power spectrum versus real frequency,  $\omega/\omega_*$ , taken at position  $x/\rho_s = 20$ .

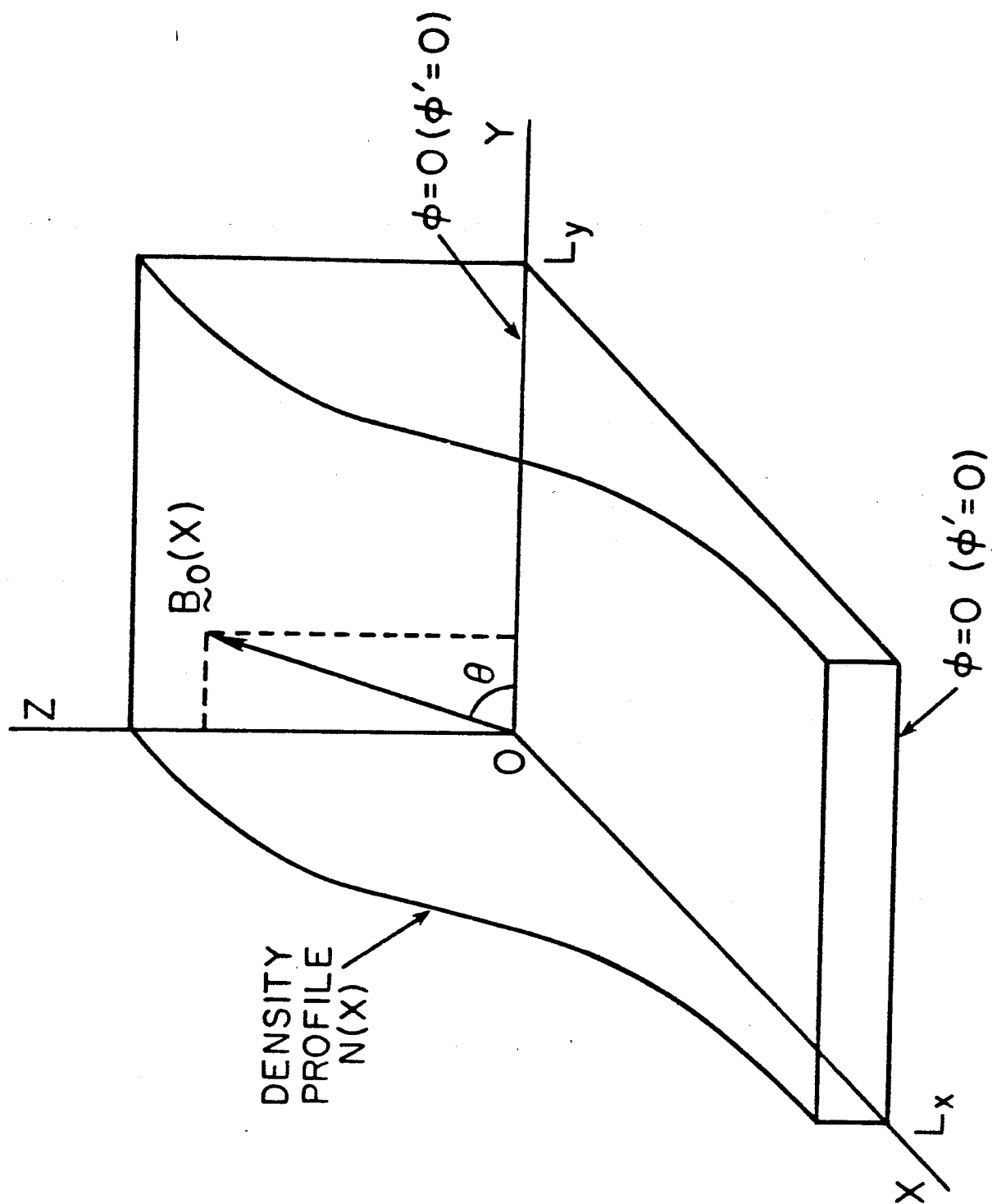


Fig. 1

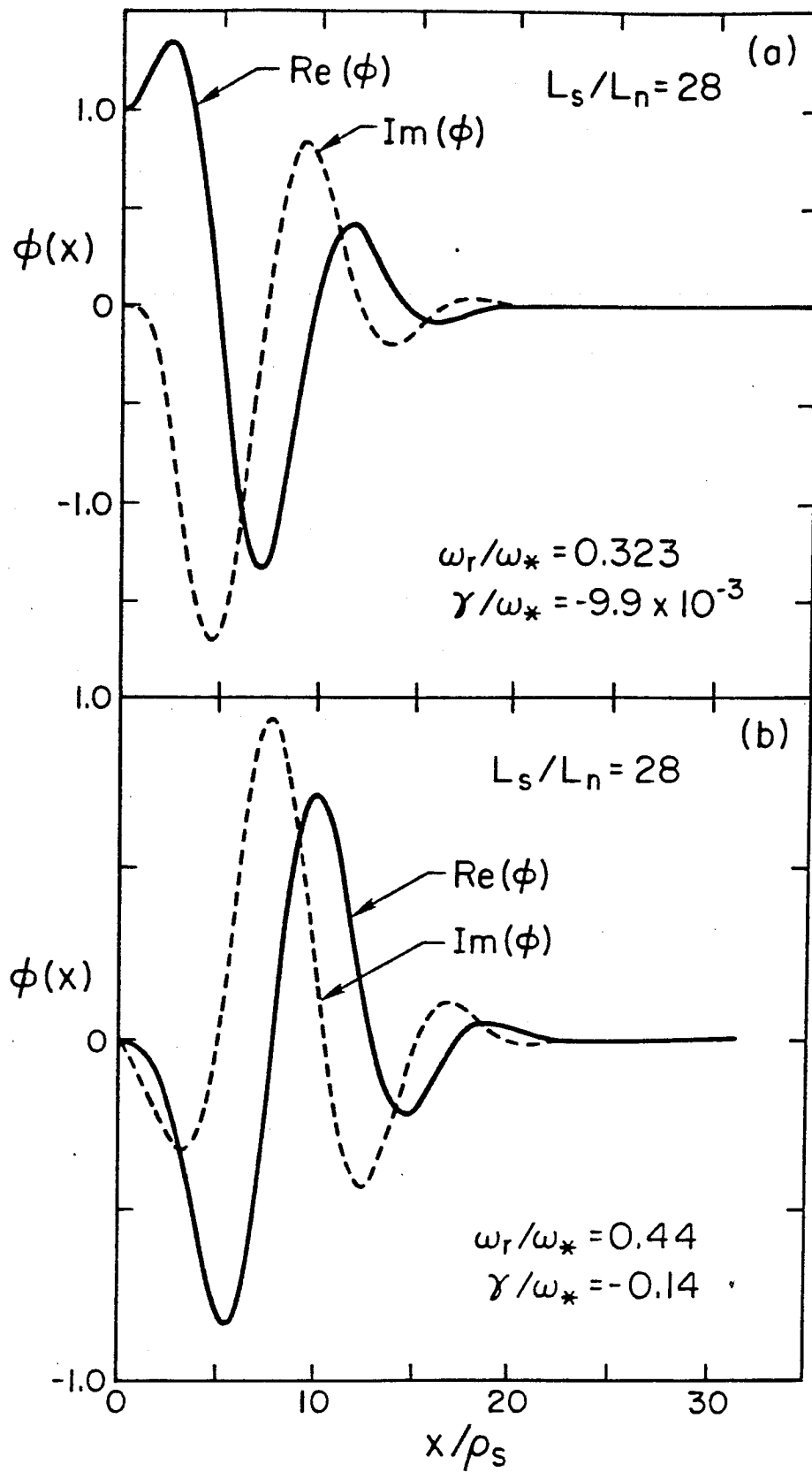


Fig. 2

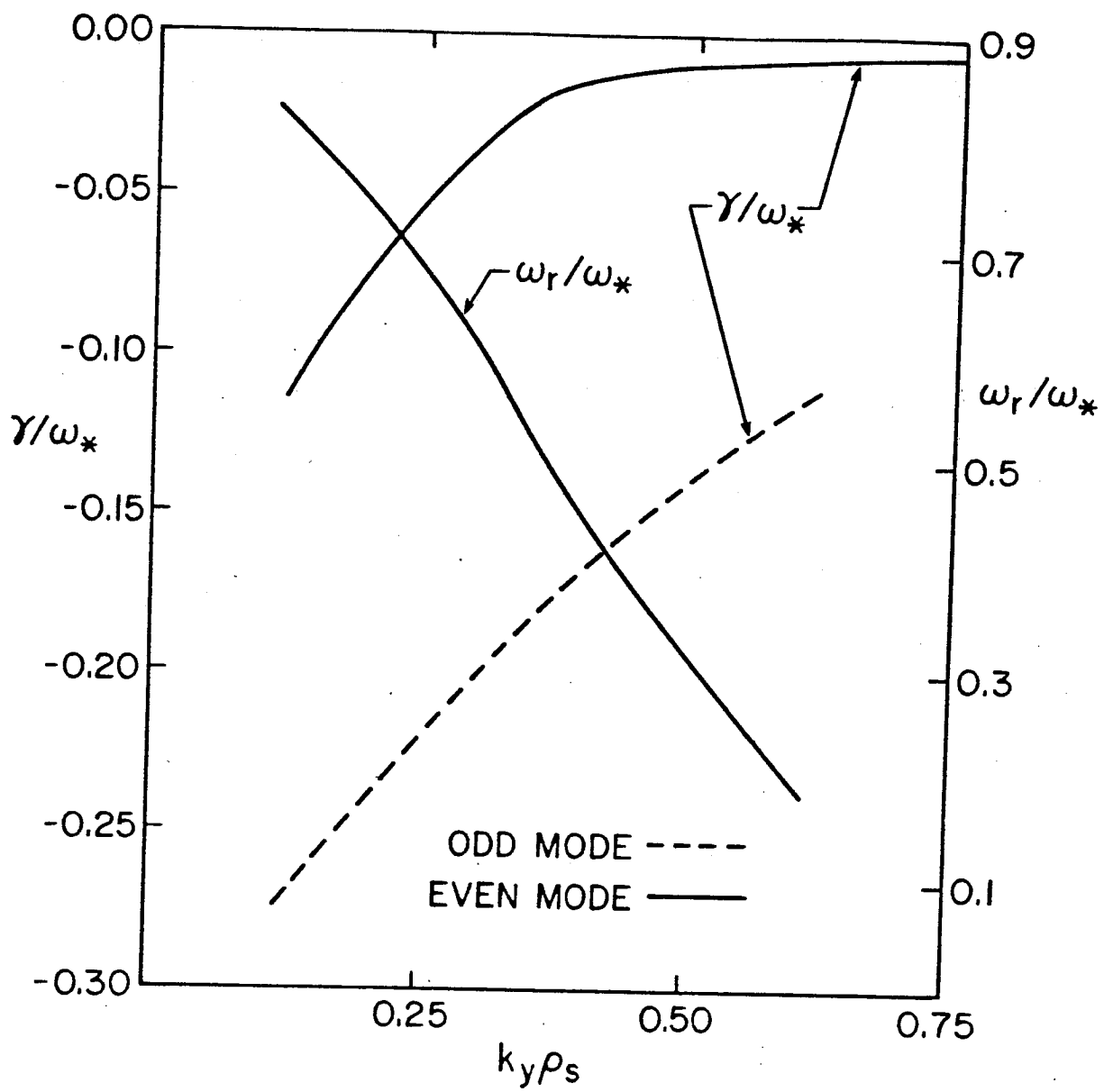


Fig. 3

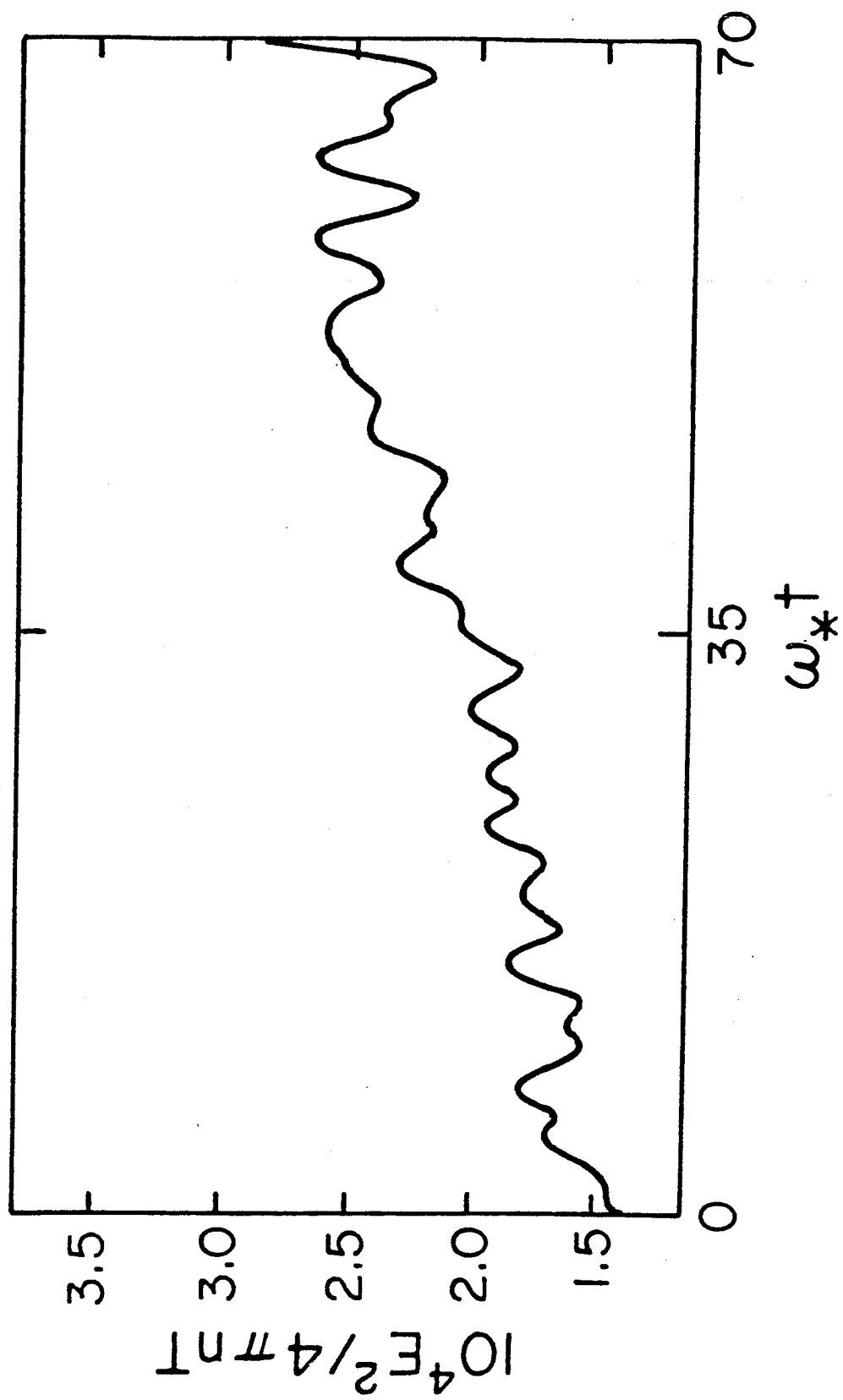


Fig. 4

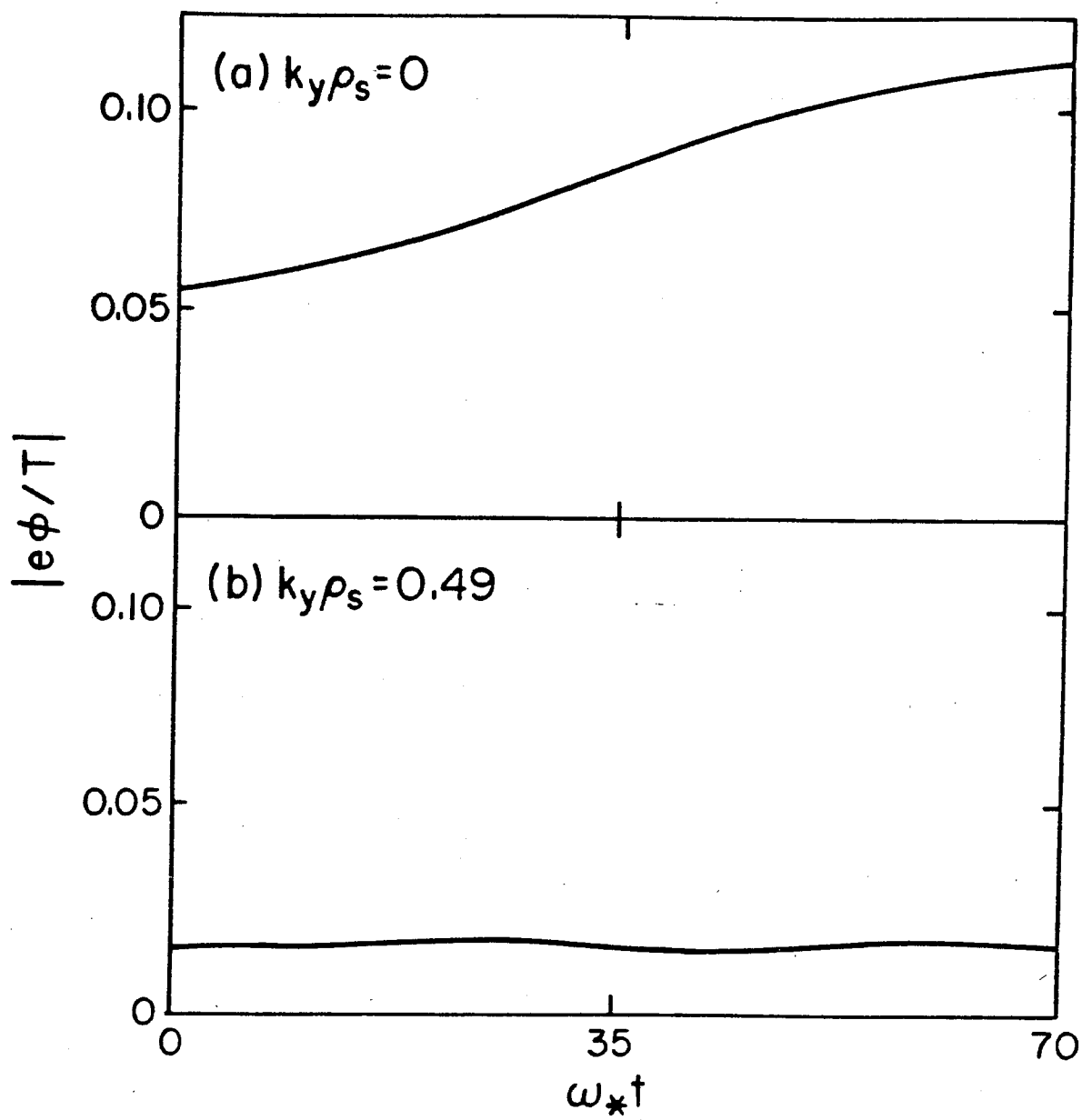


Fig. 5

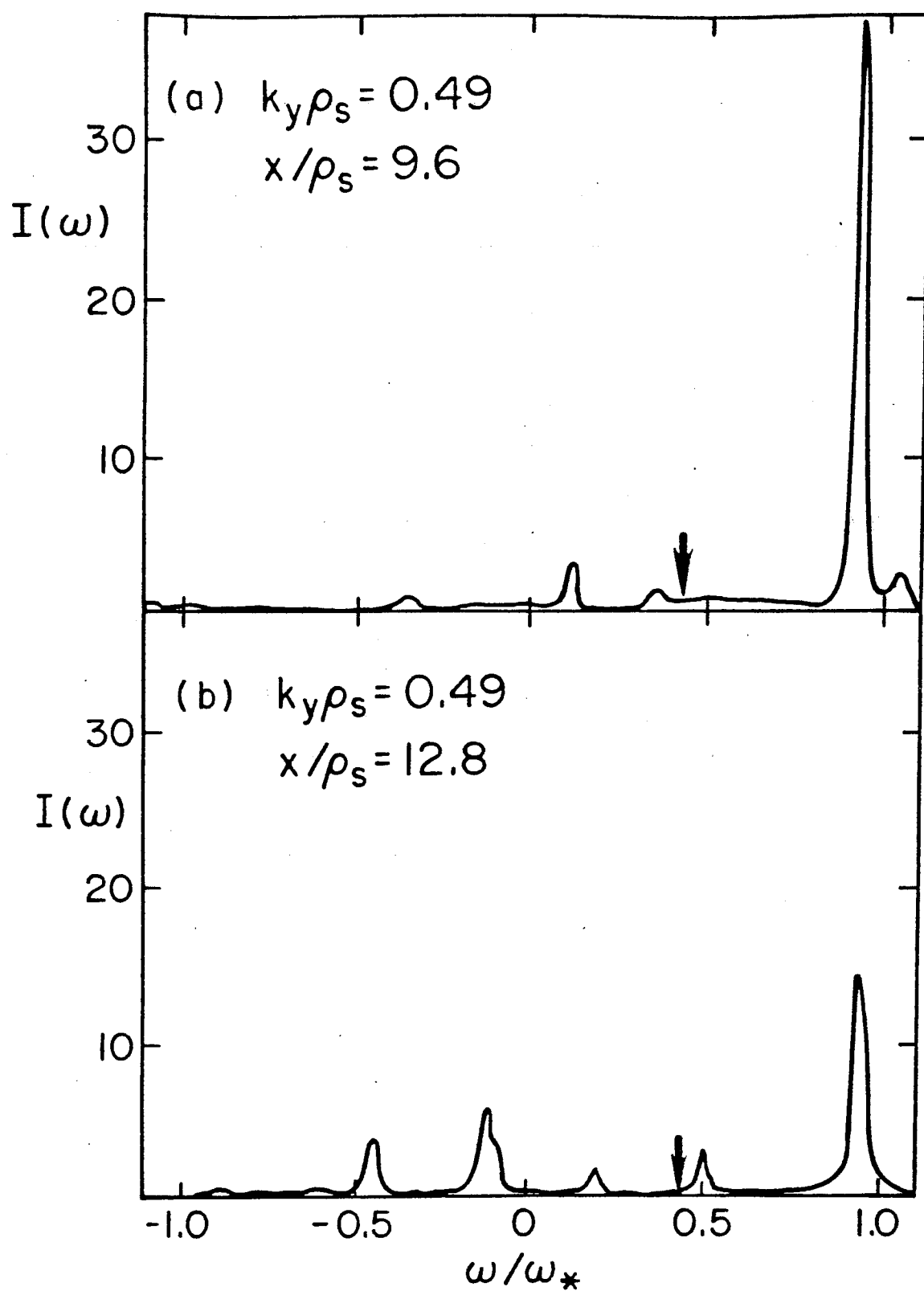


Fig. 6



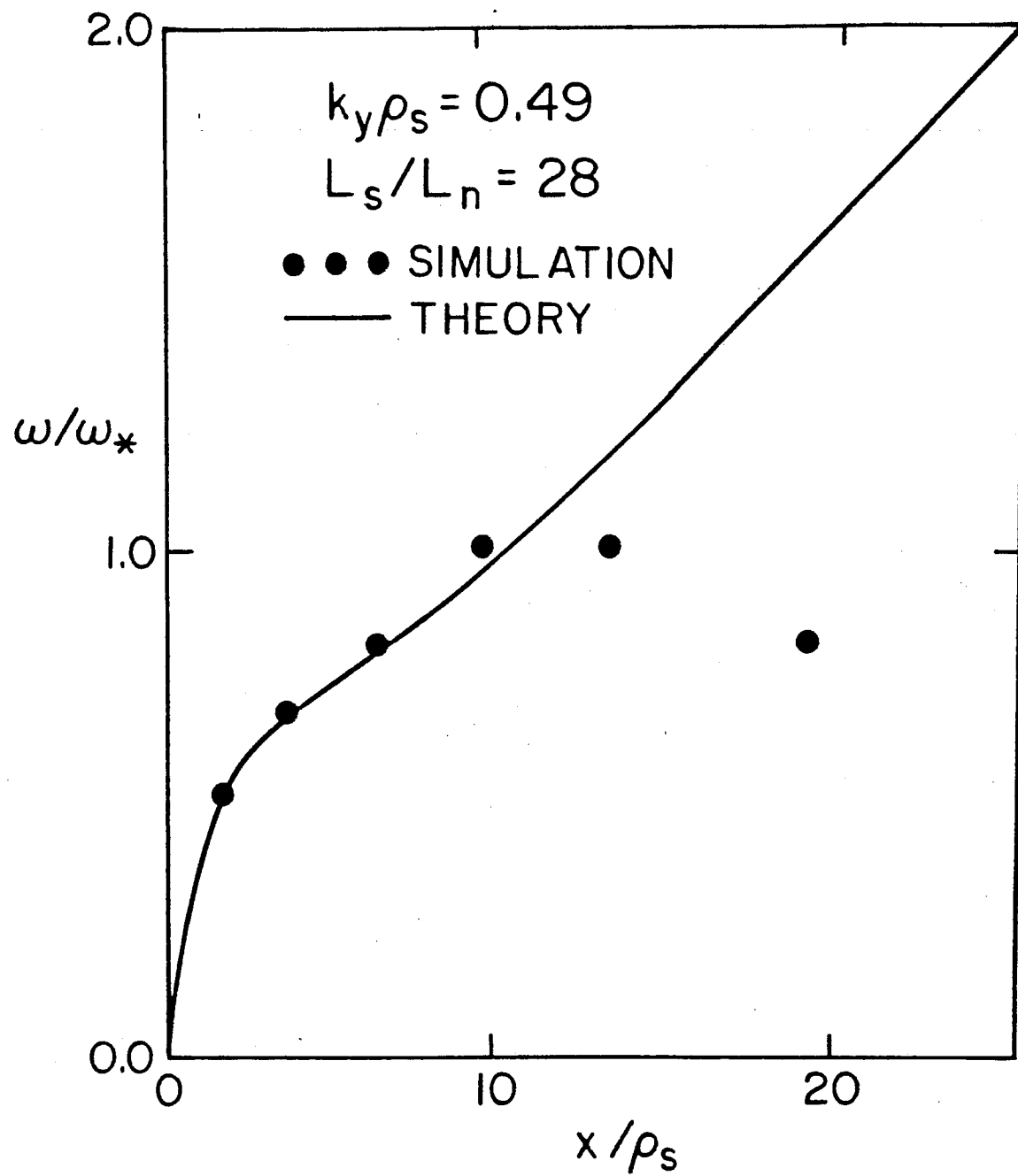


Fig. 7

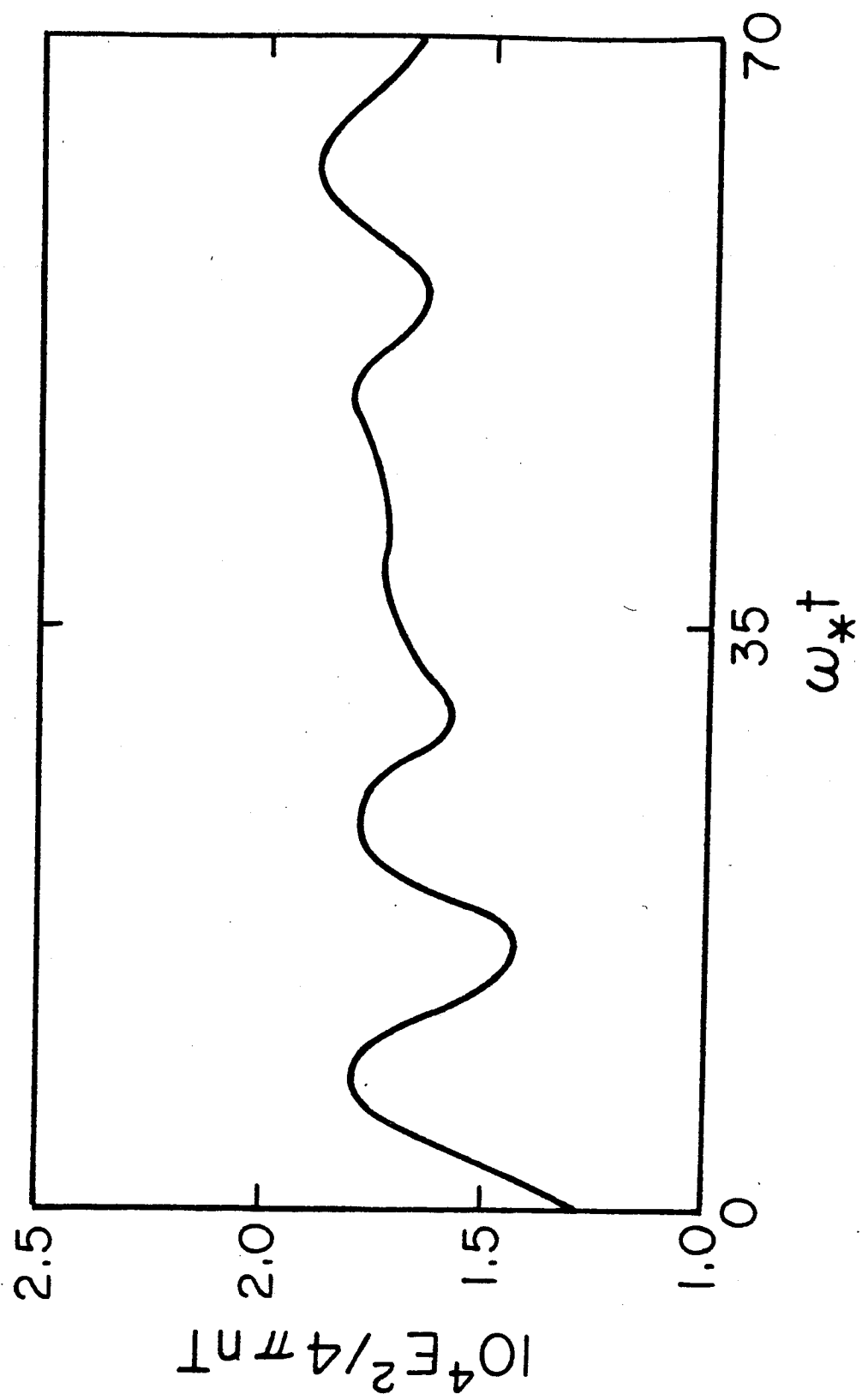


Fig. 8

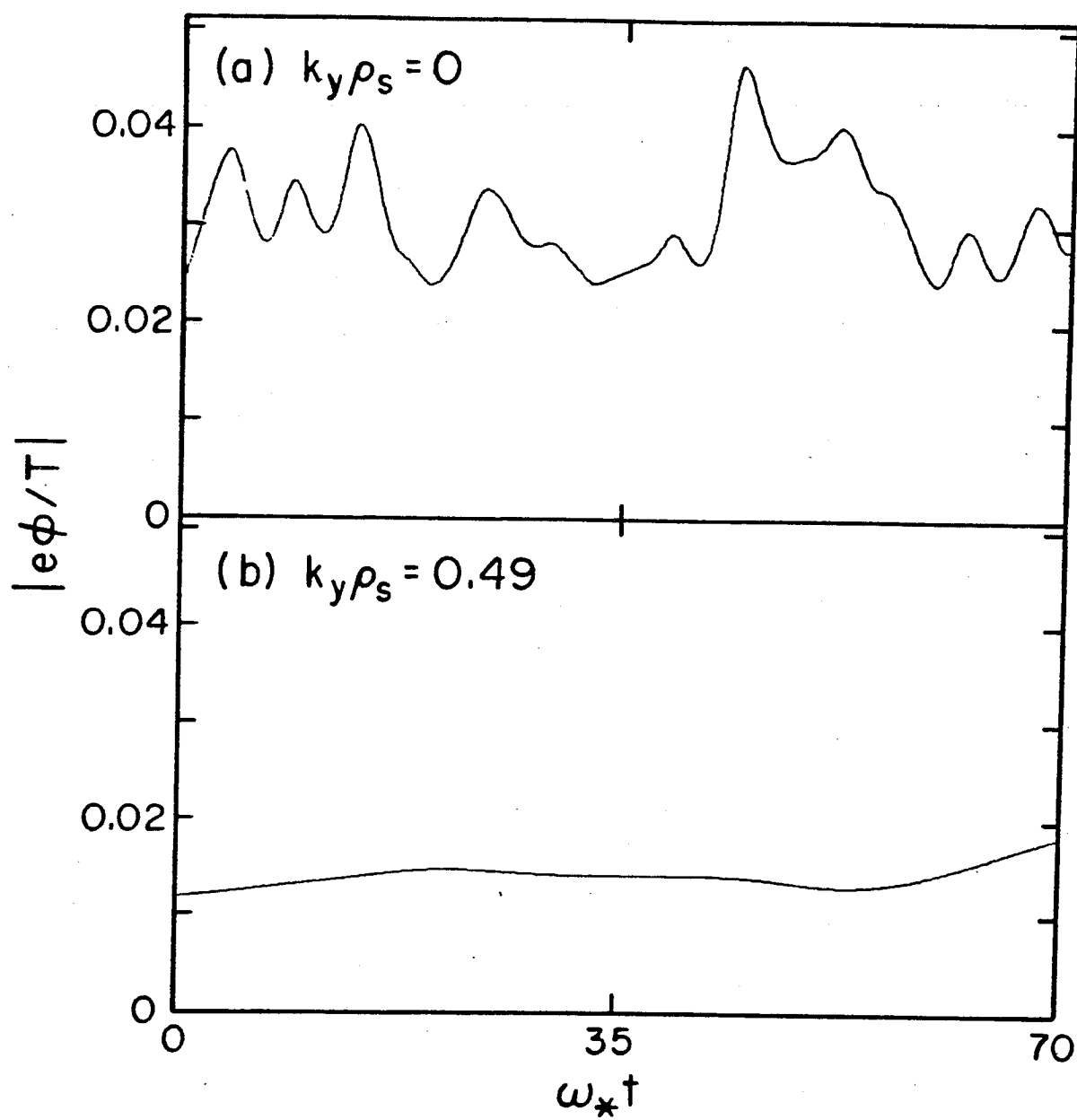


Fig. 9

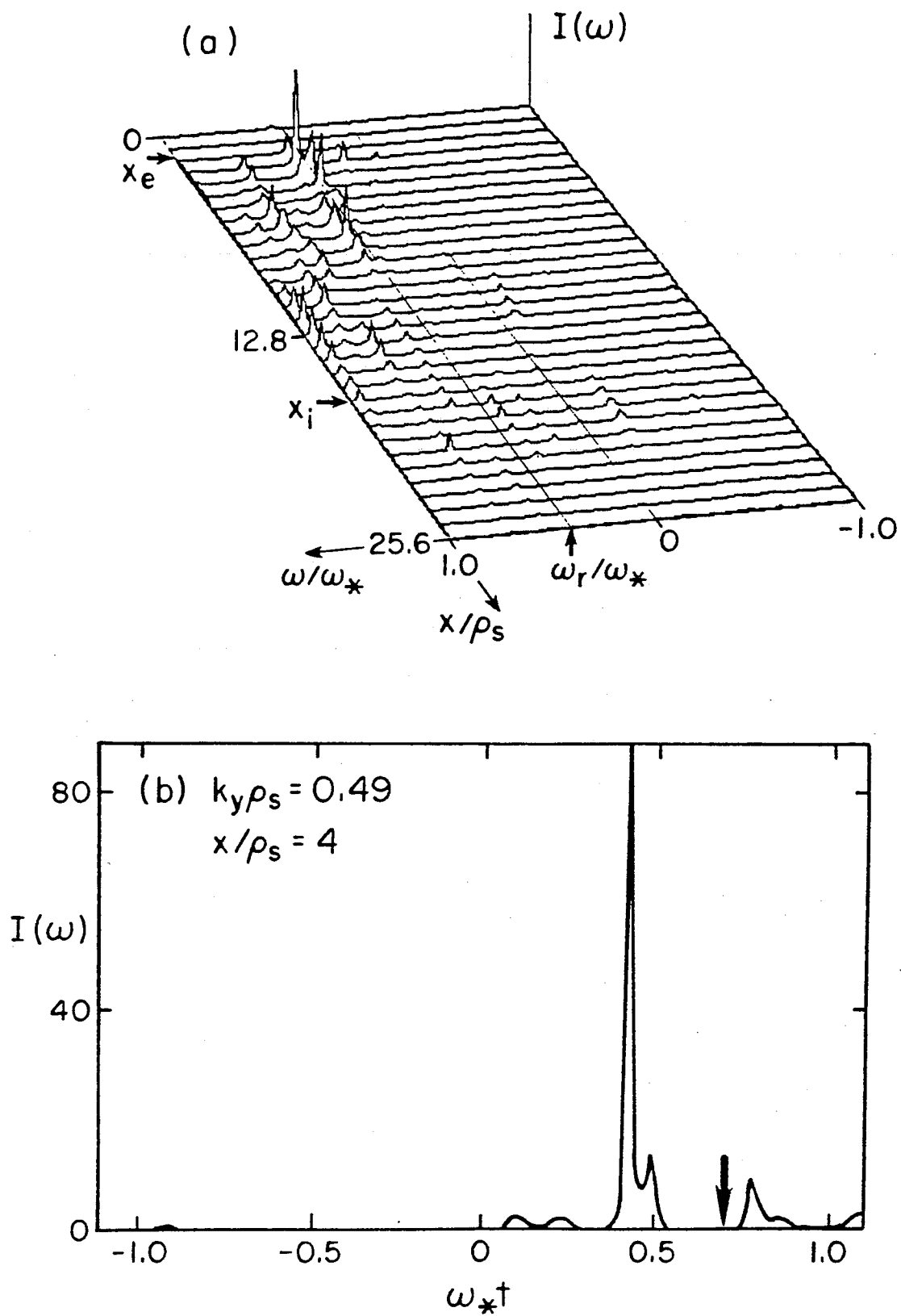


Fig. 10

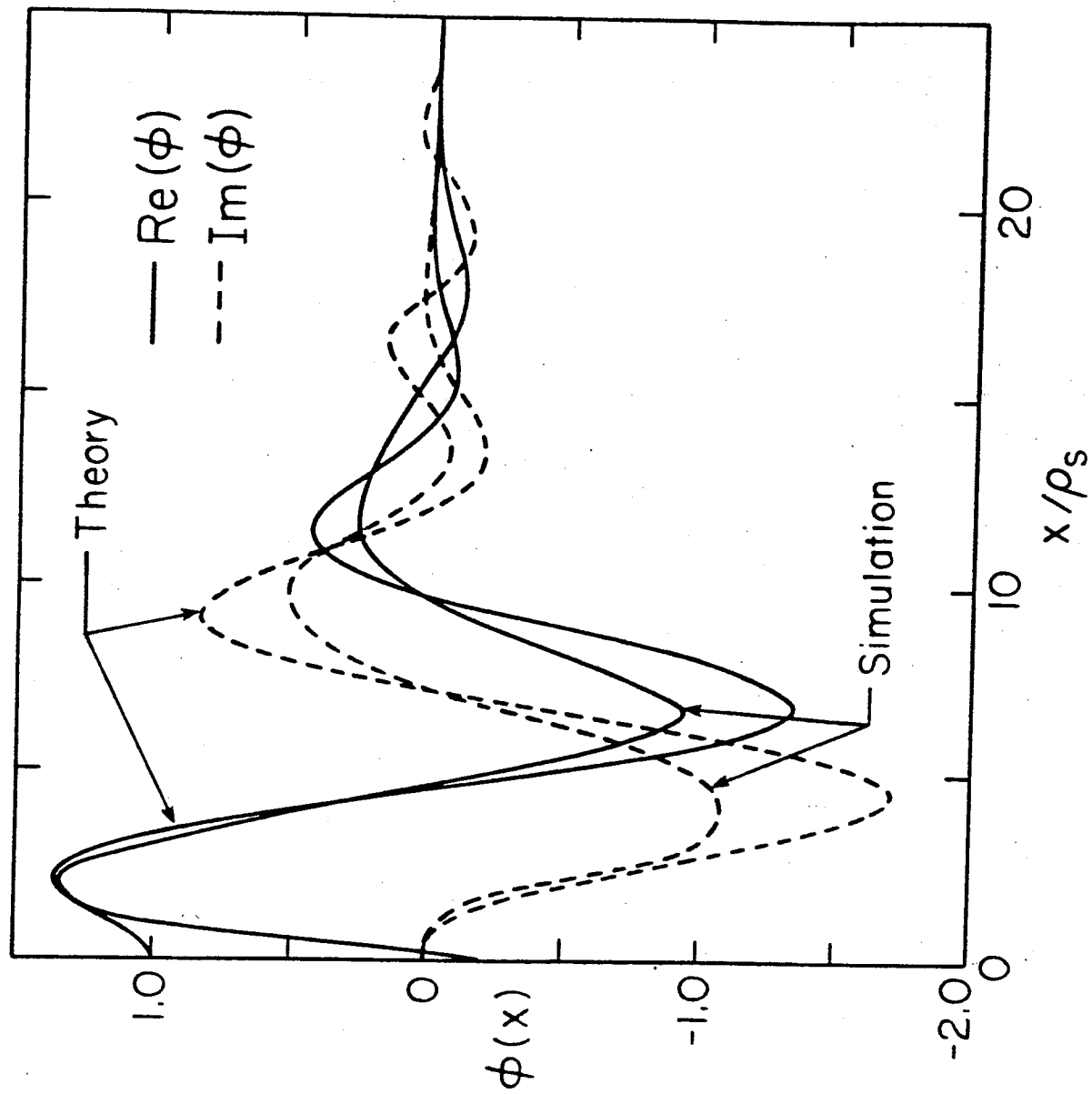


Fig. 11

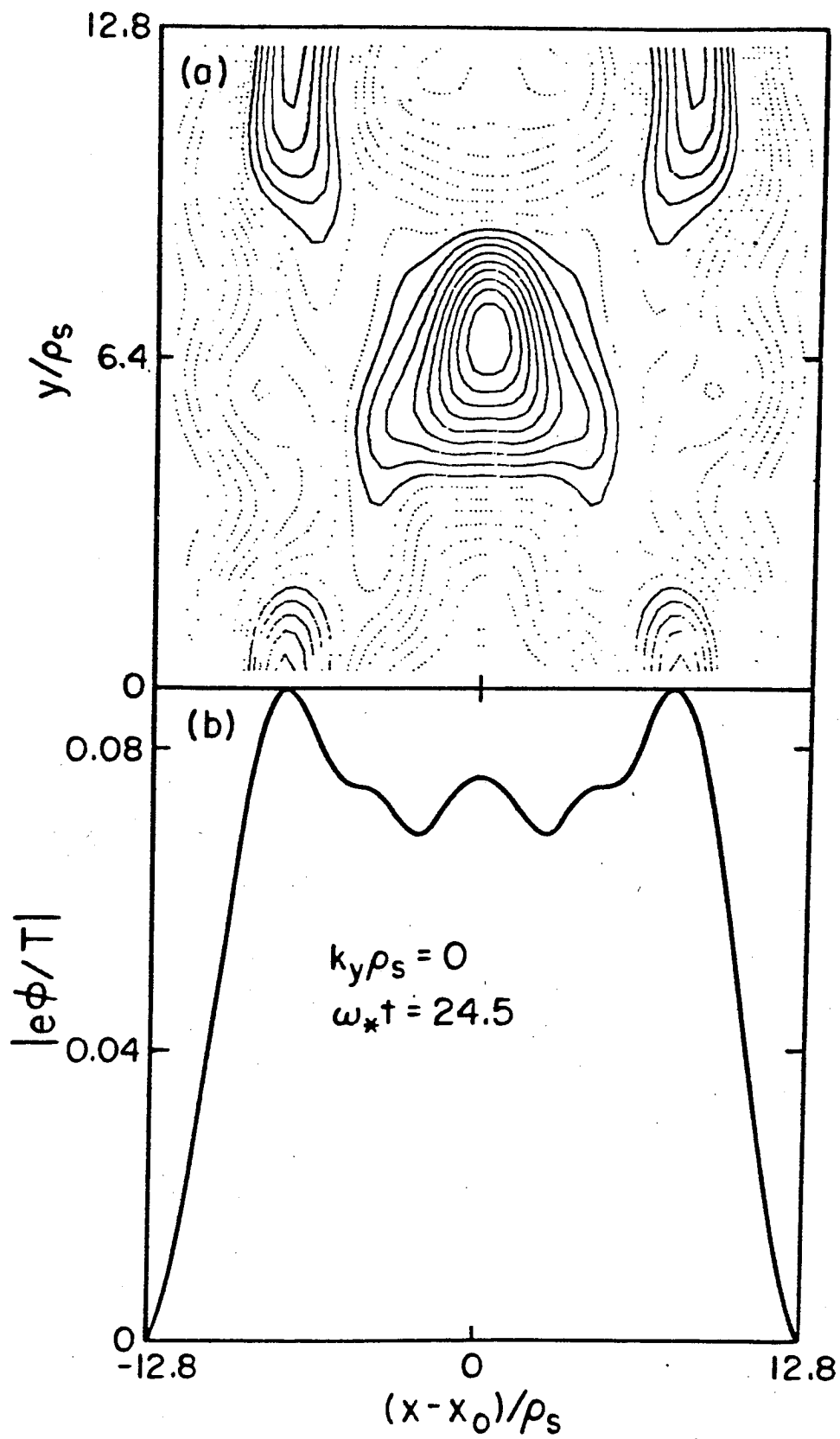


Fig. 12

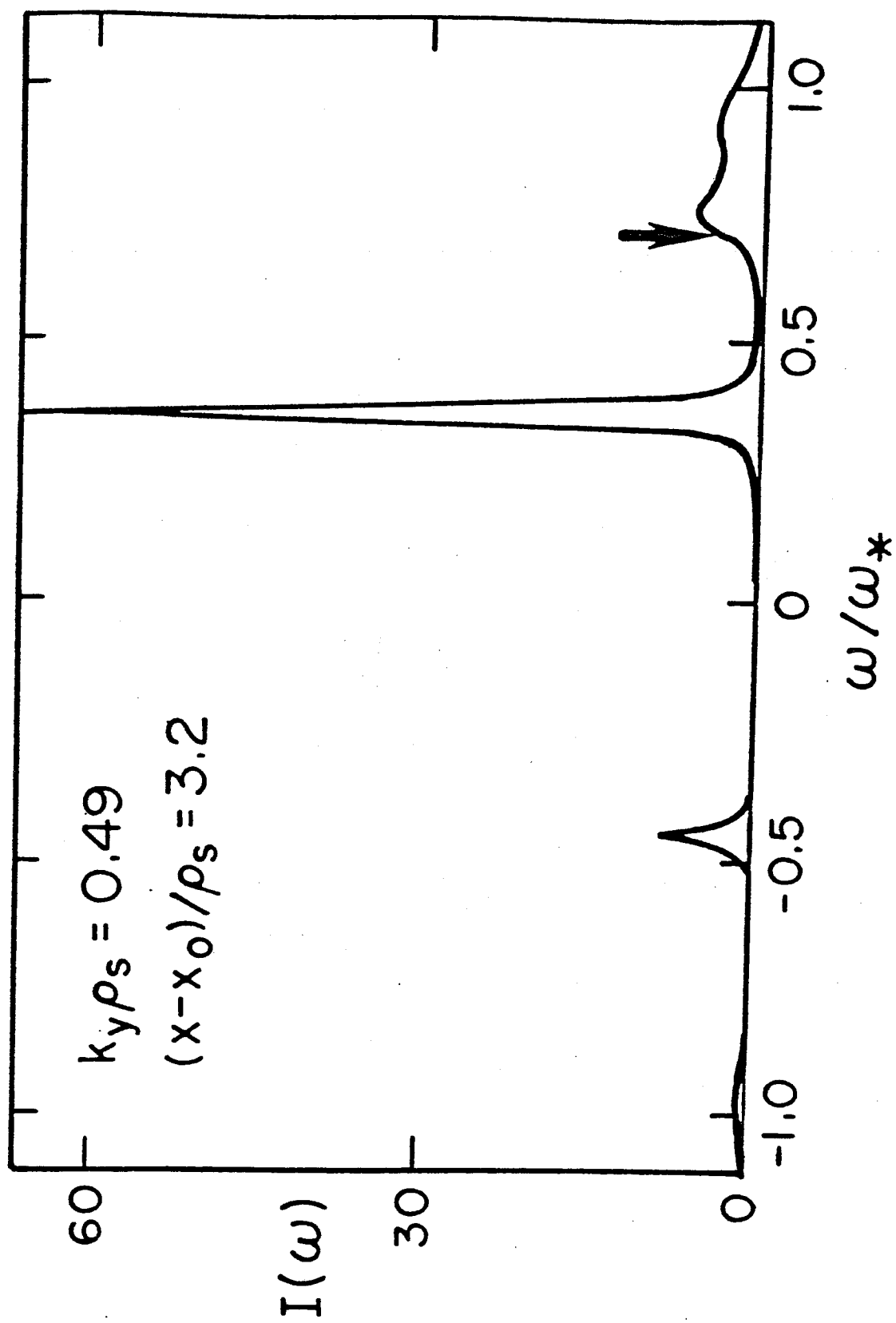


Fig. 13

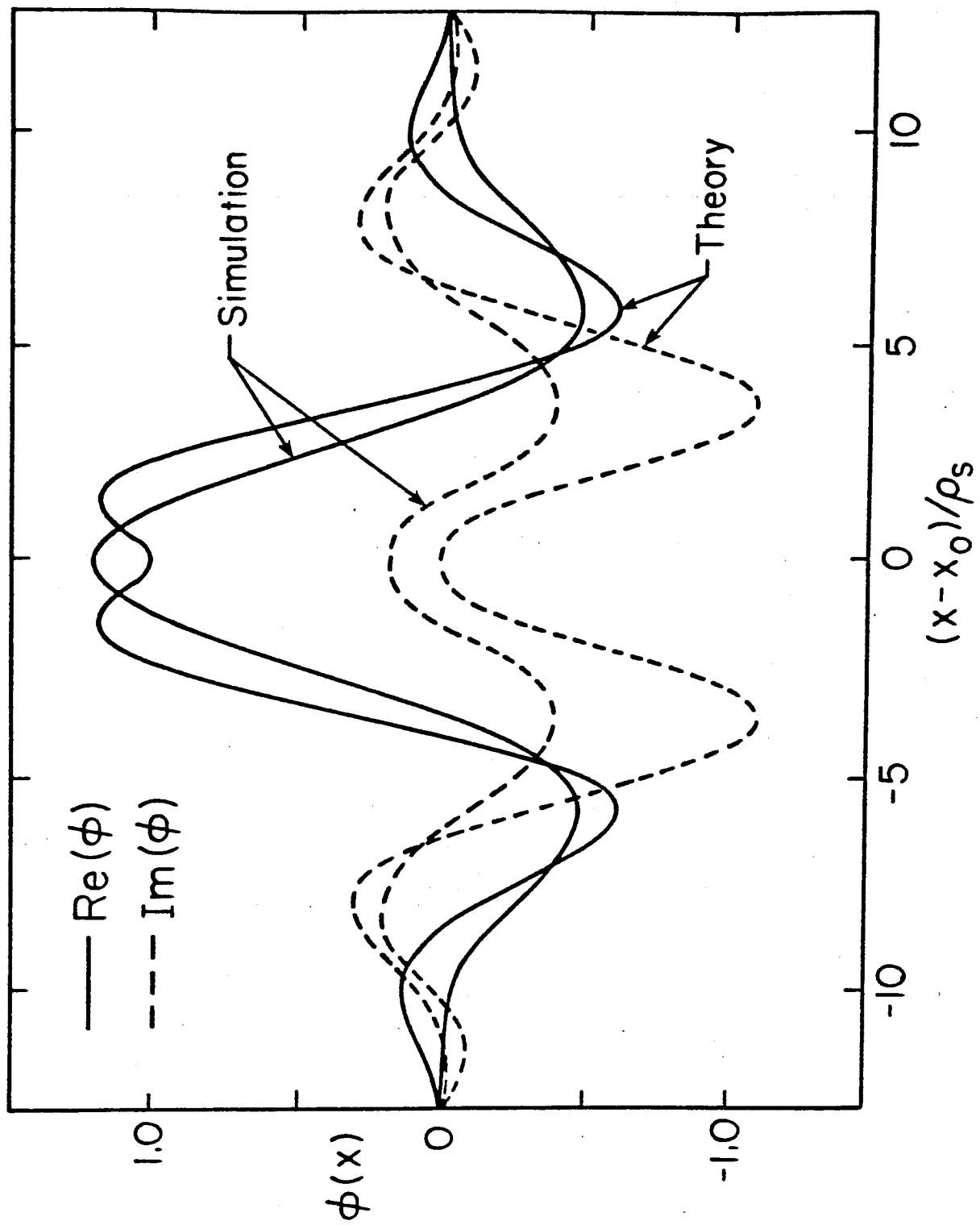


Fig. 14



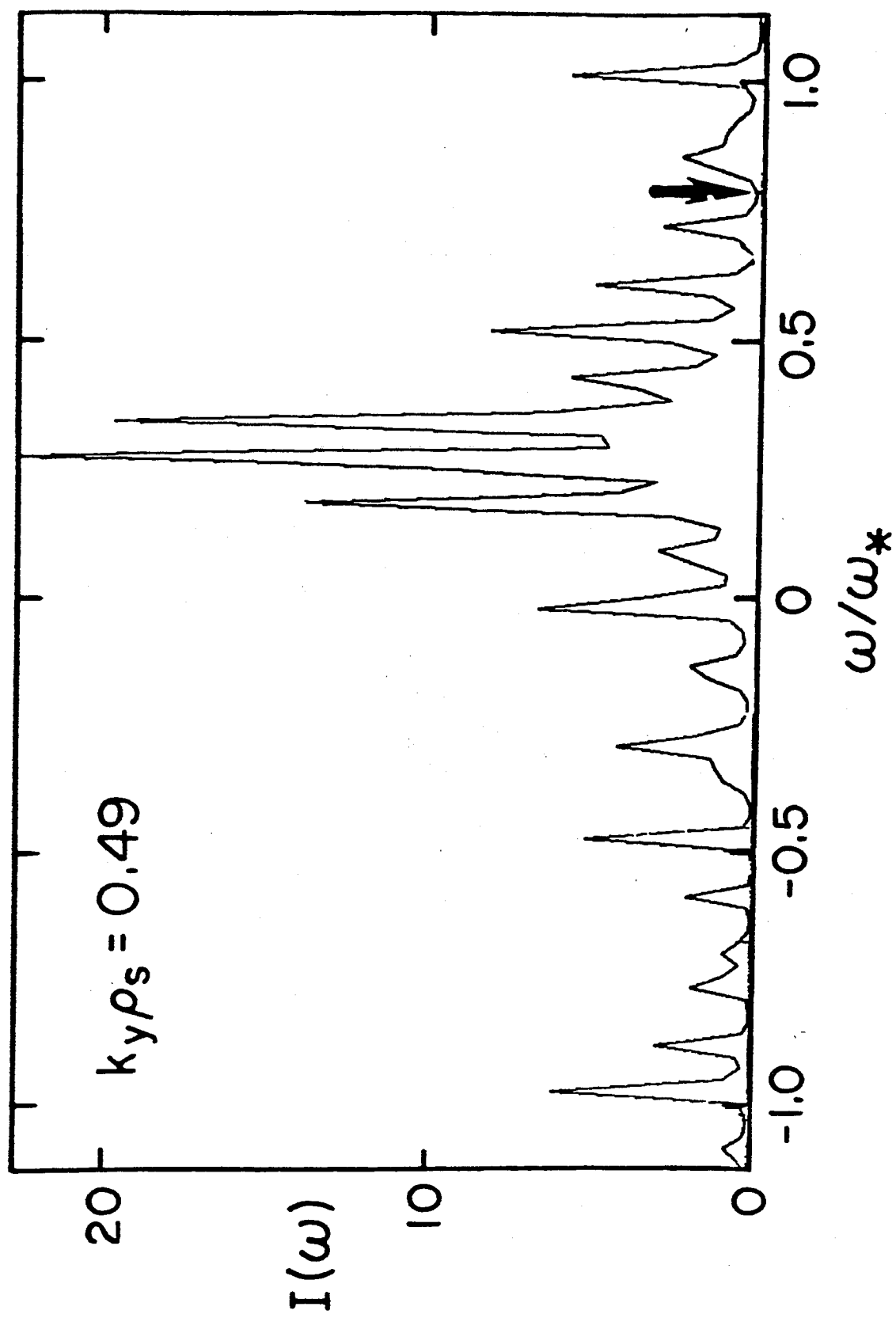


Fig. 15

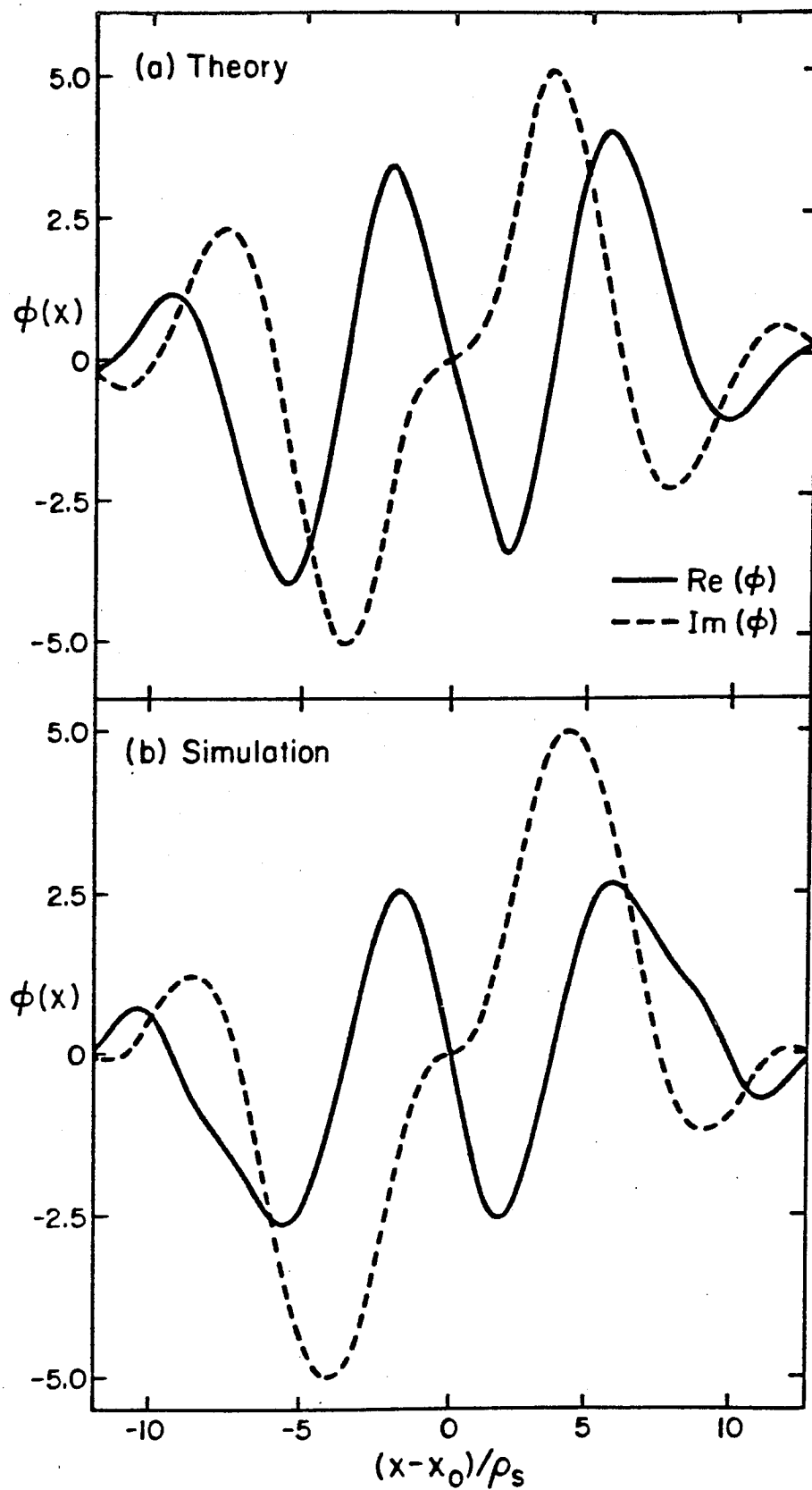


Fig. 16

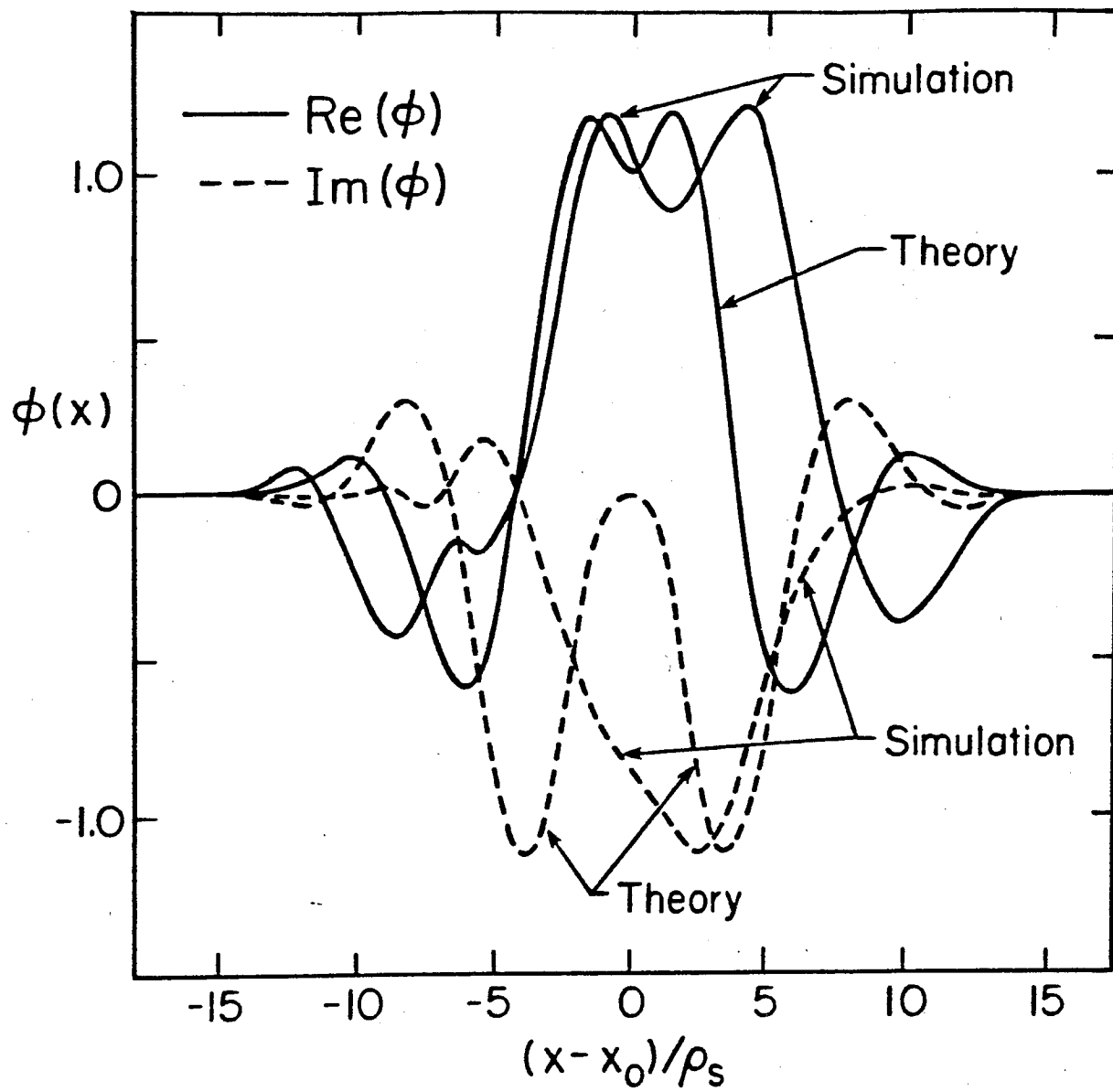


Fig. 17

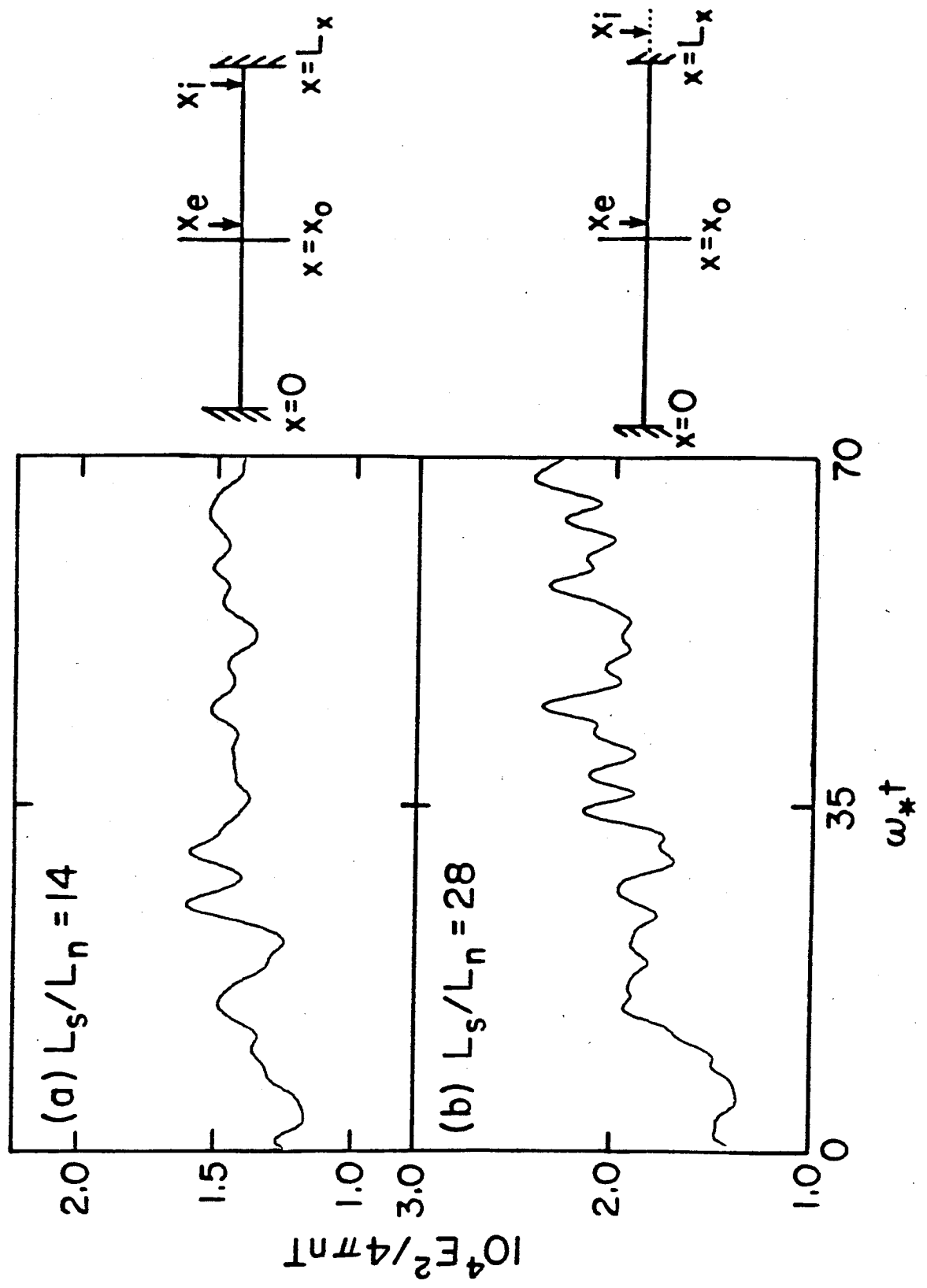


Fig. 18

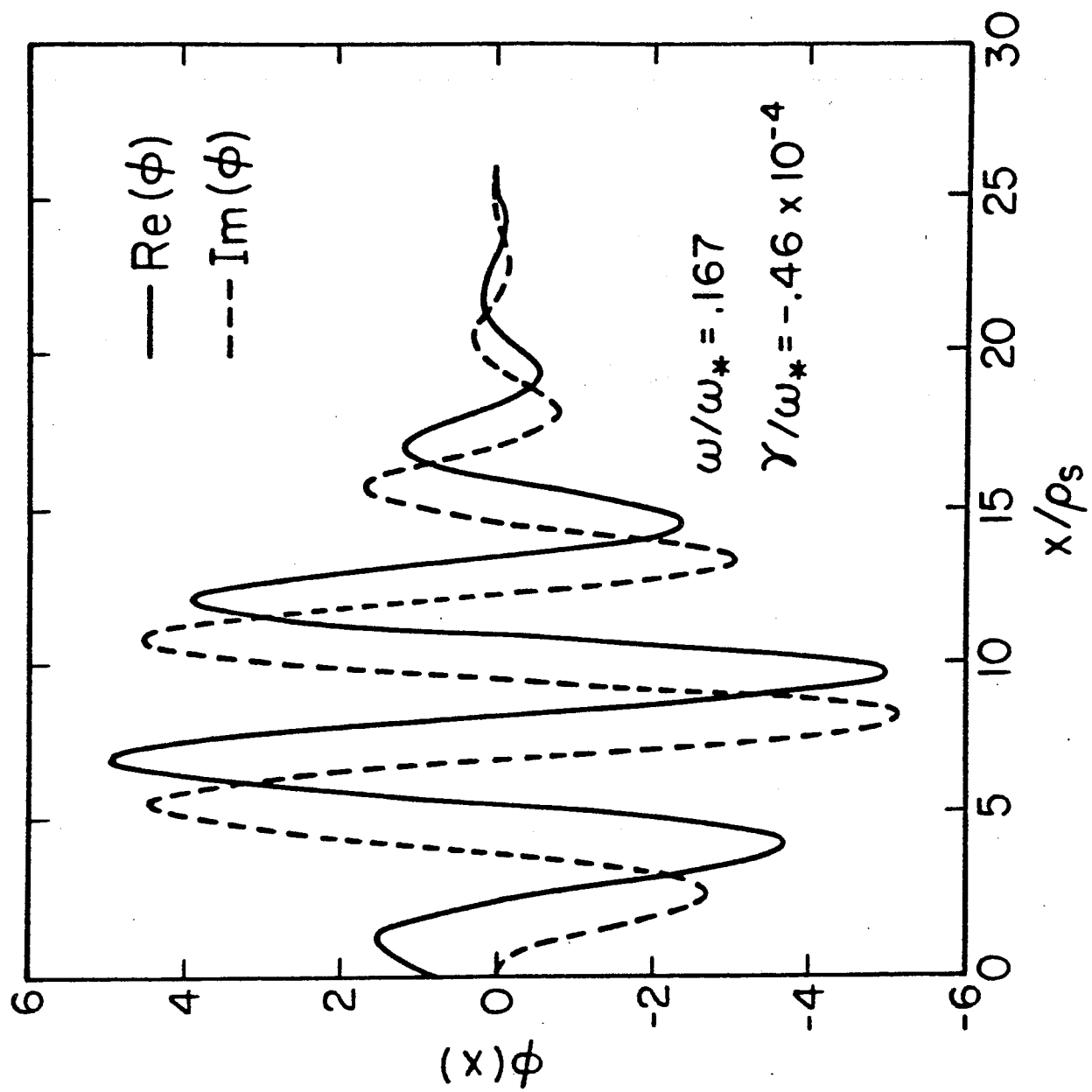


Fig. 19

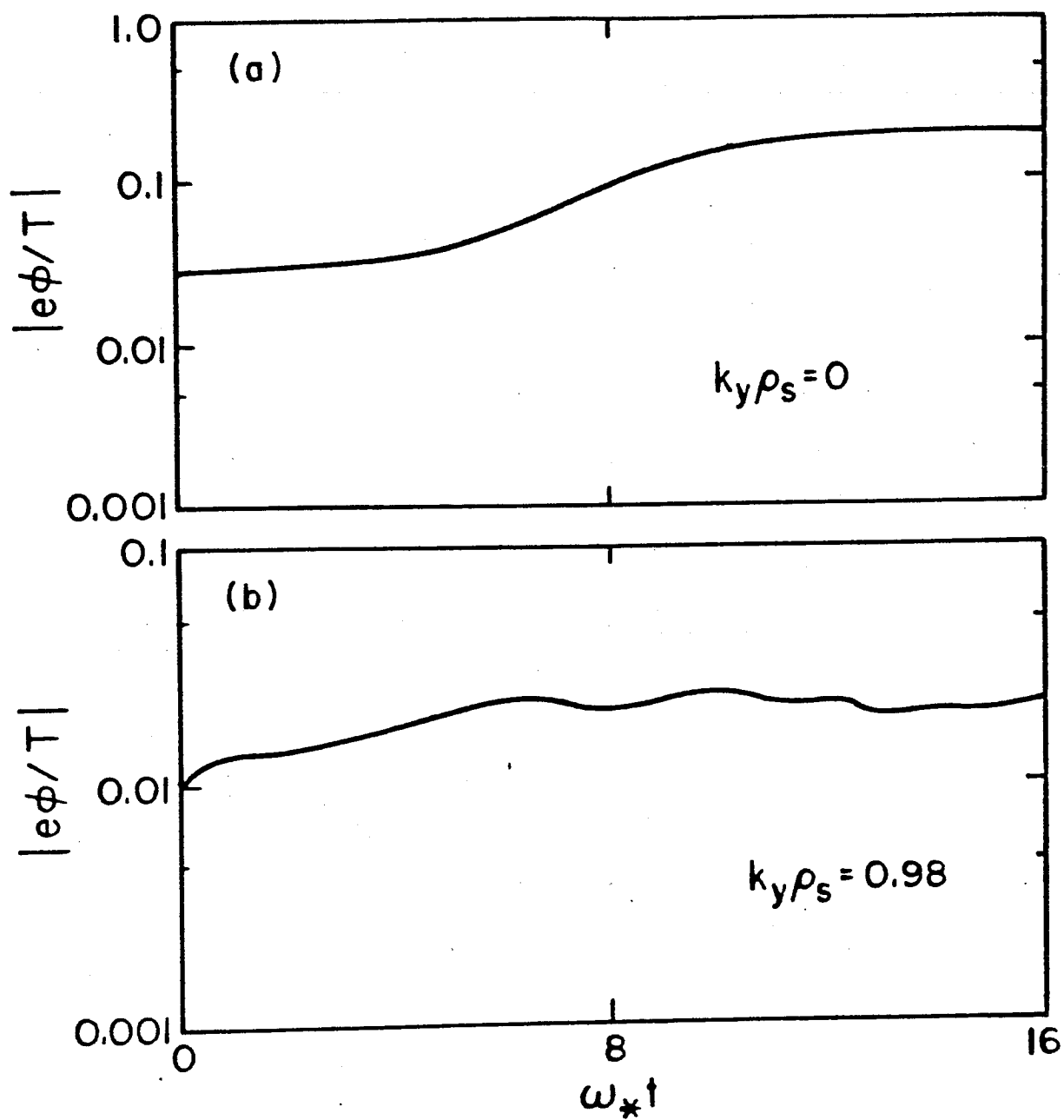


Fig. 20

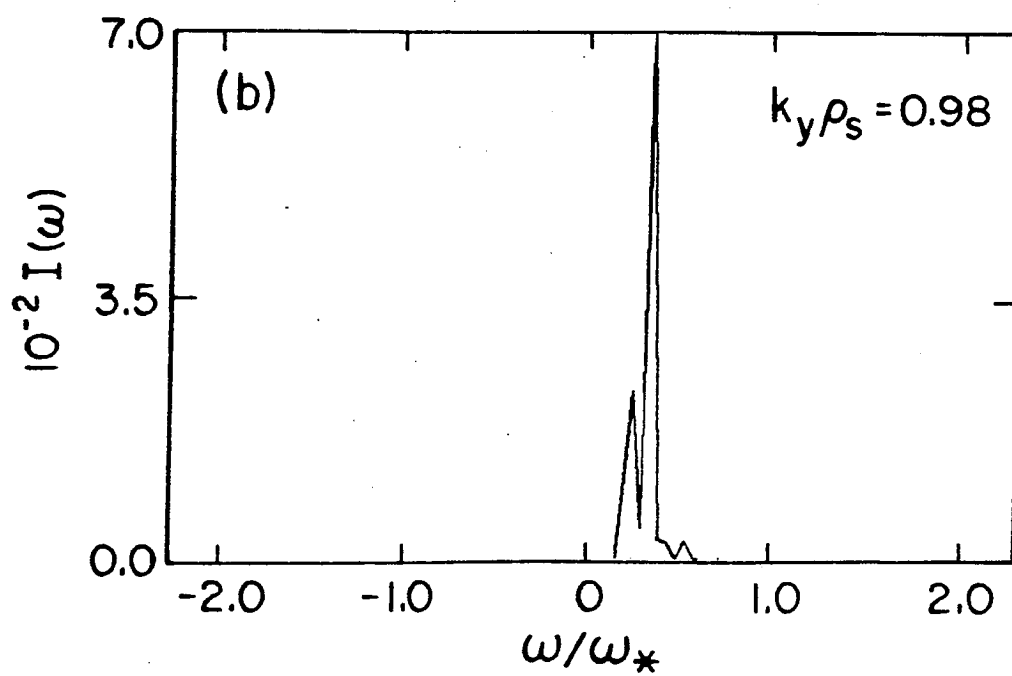
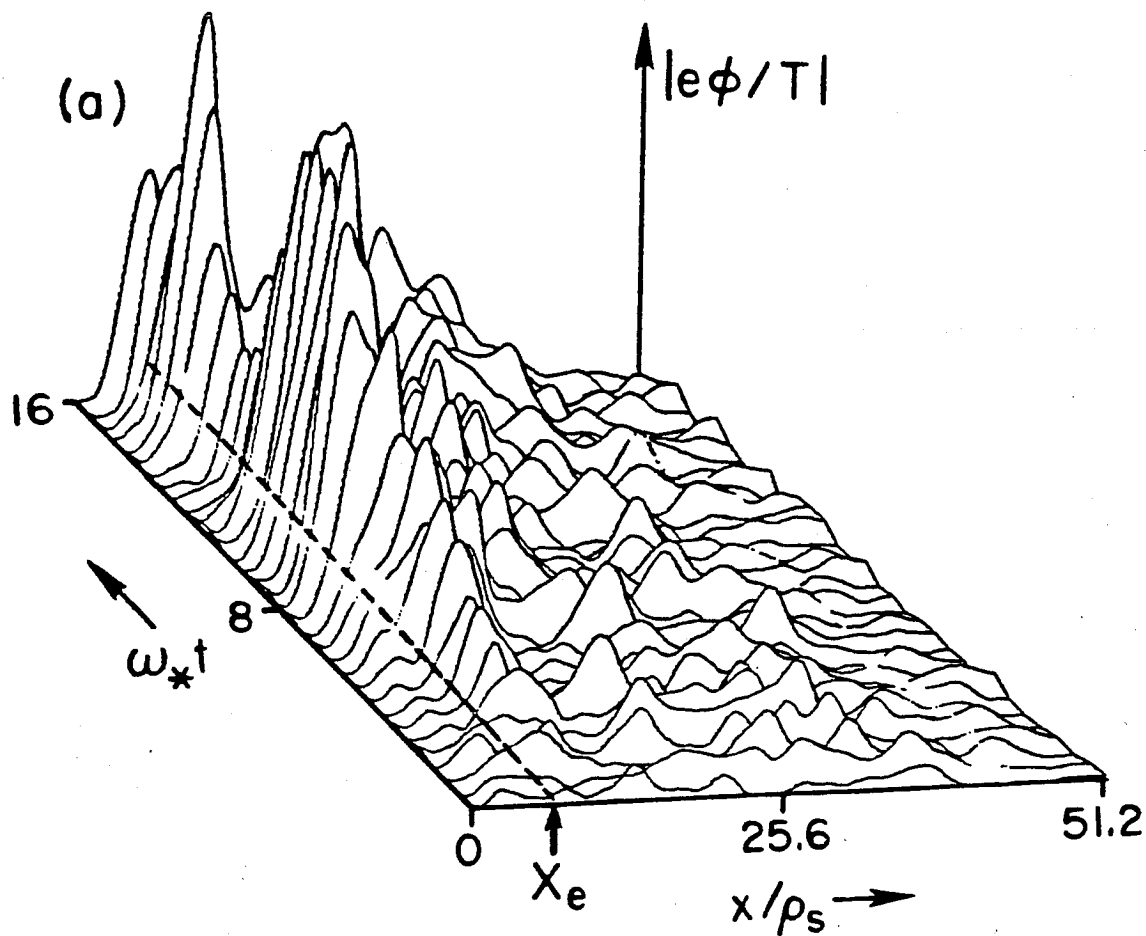


Fig. 21

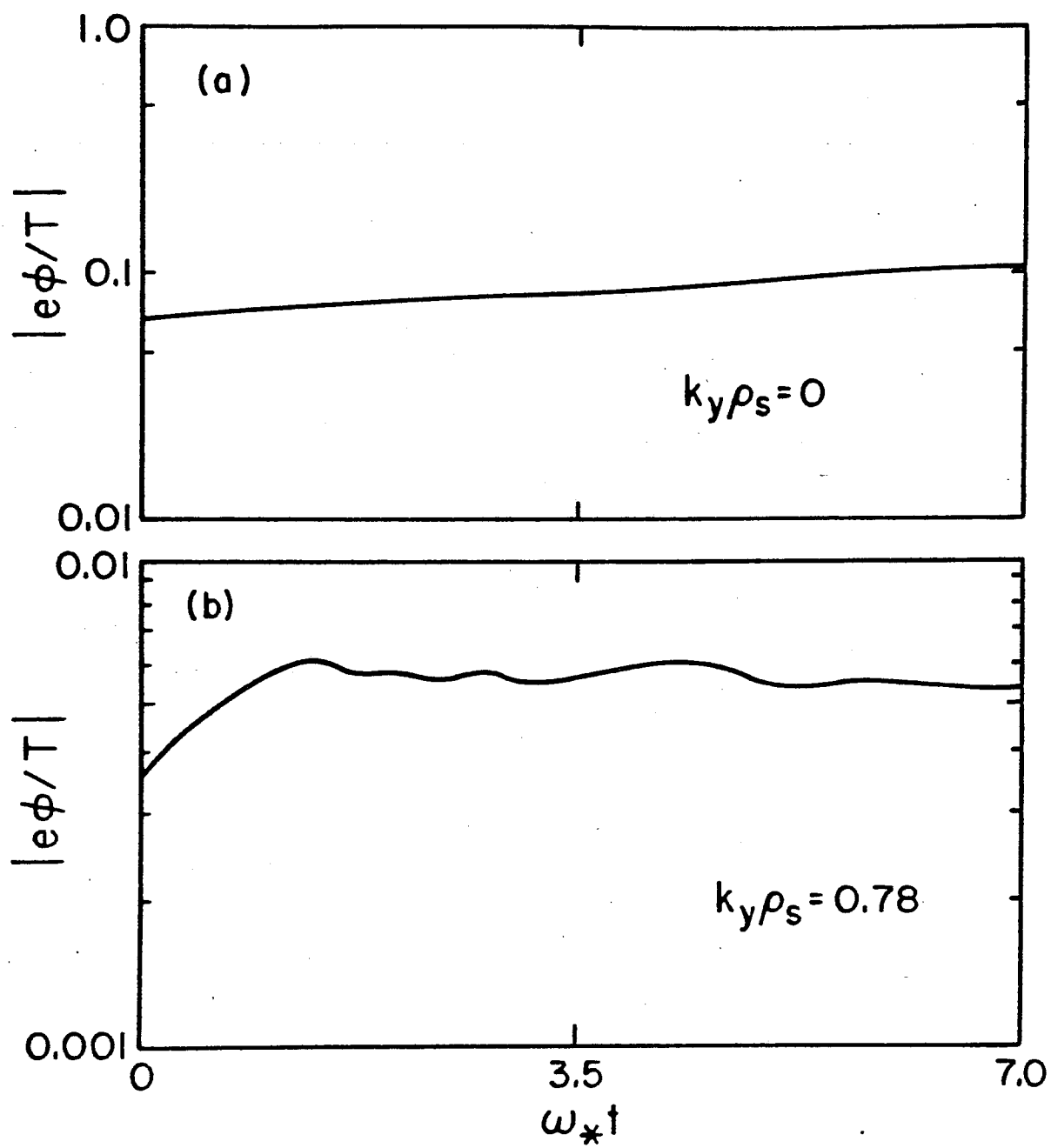


Fig. 22



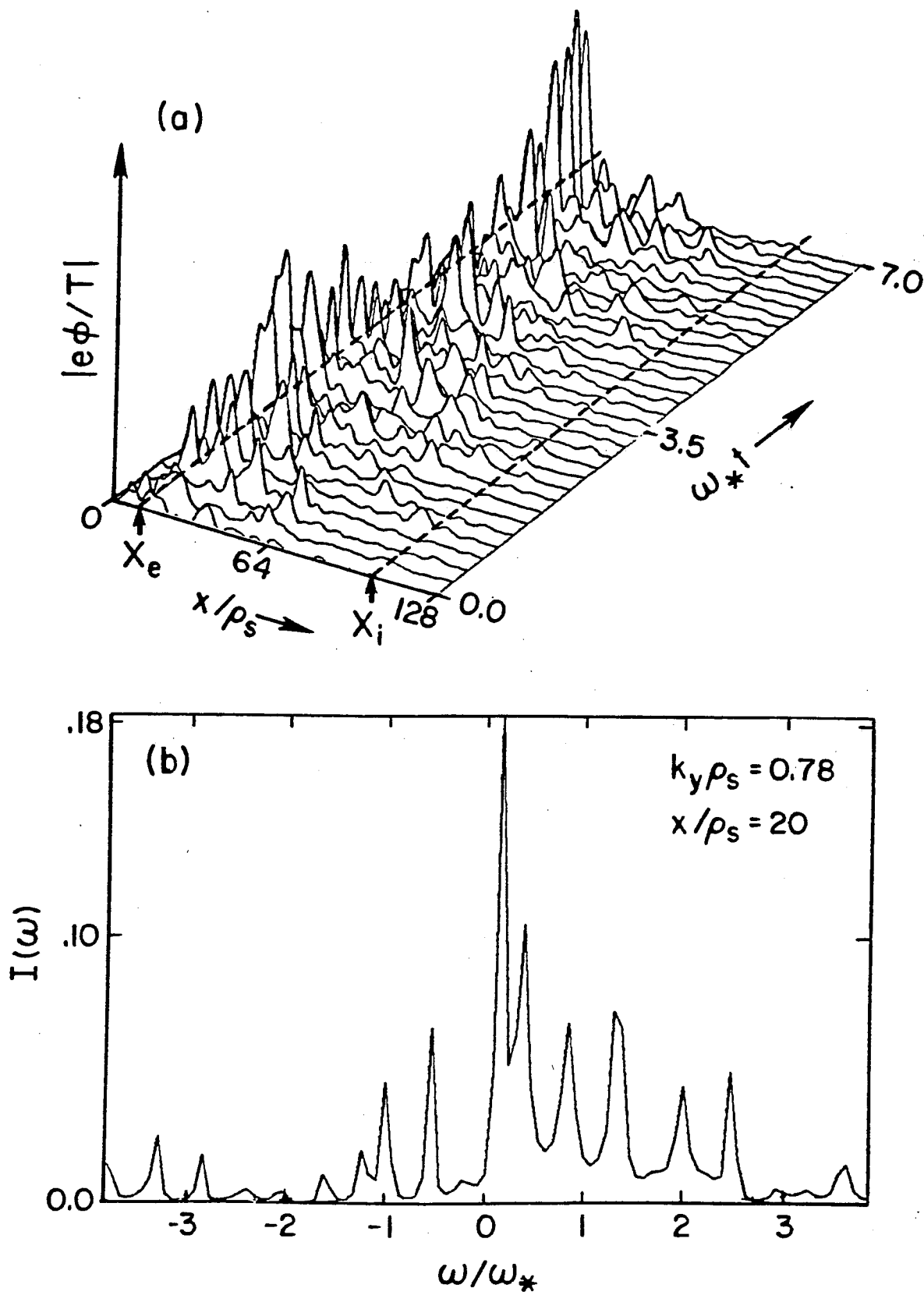


Fig. 23